# DEVELOPMENT OF WIDEBAND RADIO CHANNEL MEASUREMENT AND MODELING TECHNIQUES FOR FUTURE RADIO SYSTEMS

## Jarmo Kivinen

Dissertation for the degree of Doctor of Science in Technology to be presented with due permission for public examination and debate in Auditorium S1 at Helsinki University of Technology (Espoo, Finland) on the 2nd of March 2001 at 12 o'clock noon.

**Helsinki University of Technology**

**Department of Electrical and Communications Engineering**

**Radio Laboratory**


**Teknillinen korkeakoulu**

**Sähkö- ja tietoliikennetekniikan osasto**

**Radiolaboratorio**

## Preface

This thesis has been done at the Radio Laboratory of the Helsinki University of Technology during 6/94–2/95 and 8/96– 2/01.

*Espoo, 9. 2. 2001.*


*Jarmo Kivinen*

**Abstract**

This thesis discusses the development of micro- and millimeterwave wideband radio channel measurement and modeling techniques for future radio networks. Characterization of the radio channel is needed for radio system, wireless network, and antenna design. A radio channel measurement system was designed for 2.154, 5.3 GHz and 60 GHz center frequencies, and completed at the two lower frequencies. The sounder uses a pseudonoise code in the transmitter. In the receiver, first a sliding correlator, and later direct digital sampling, where the impulse response is detected by digital post processing, were realized. Certain implementation questions, like link budget, effects of phase noise on impulse response and direction of arrival estimation, and achievable performance using the designed concept, are discussed.

Measurement campaigns included in this thesis were realized at 5.3 GHz frequency in micro- and picocells. A comprehensive measurement campaign performed inside different buildings was thoroughly analyzed. Propagation mechanisms were studied and empirical models for both large scale fading and multipath propagation were developed. Propagation through walls, diffraction through doorways, and propagation paths outside the building were observed. Pathloss in LOS was lower than the free space pathloss, due to wave guiding effects. In NLOS situation difference in the pathloss models in different buildings was significant. Behavior of the spatial diversity was estimated on the basis of spatial correlation functions extracted from the measurement data; an antenna separation of a fraction of a wavelength gives sufficient de-correlation for significant diversity gain in indoor environments at 5.3 GHz in NLOS.

# Contents

**List of publications**

[P1]    J. Kivinen, T. Korhonen, P. Aikio, R. Gruber, P. Vainikainen, and S. -G. Häggman, "Wideband radio channel measurement system at 2 GHz," *IEEE Transactions on Instrumentation and Measurement*, vol. 48, No. 1, 1999, pp. 39–44.

[P2]    J. Kivinen and P. Vainikainen, "Phase noise in a direct sequence based channel sounder," *International Symposium on Personal, Indoor and Mobile Radio Communications Proceedings*, Helsinki, Sept. 1–4, 1997, pp. 1115–1119.

[P3]    J. Kivinen and P. Vainikainen, "Calibration scheme for synthesizer phase fluctuations in virtual antenna array measurements," *Microwave and Optical Technology Letters*, vol. 26, No. 3, 2000, pp. 183–187.

[P4]    J. Kivinen and P. Vainikainen, "Wideband indoor radio channel measurements at 5.3 GHz," *27$^{th}$ European Microwave Conference Proceedings*, Jerusalem, Israel, Sept. 8–12, 1997, pp. 464–469.

[P5]    J. Kivinen, X. Zhao, and P. Vainikainen, "Wideband indoor radio channel measurements with direction of arrival estimations in the 5 GHz band," *IEEE VTS 50$^{th}$ Vehicular Technology Conference Proceedings*, Amsterdam, Netherlands, Sept. 19–22, 1999, pp. 2308–2312.

[P6]    J. Kivinen, X. Zhao, and P. Vainikainen, "Empirical characterization of wideband indoor radio channel at 5.3 GHz," to be published in *IEEE Transactions on Antennas and Propagation,* May 2001, vol. 49, 10 p.

[P7]    K. Skog, A. Brehonnet, H. Kauppinen, and J. Kivinen, "Wideband radio channel outdoor measurements at 5.3 GHz," *AP 2000 Millennium Conference on Antennas and Propagation Proceedings*, CD-ROM SP-444 (ISBN 92-9092-776-3), Davos, Switzerland, April 9–14, 2000, session 2p7, paper No. 1437.

In [P1] this author had the main responsibility of developing the measurement system in block diagram level, which is also documented in [1], and designed and constructed the following units of the system: RF-front end, IF-stage, sliding correlator (SC), and synthesizer unit. This author prepared the manuscript, except sections III C and IV B, which were originally written by Ralf Gruber and Timo Korhonen, respectively. Pauli Aikio and Ralf Gruber performed the measurements described in Section V. The work of this author was supervised by Pertti Vainikainen. In papers [P2], [P3], [P4], and [P5] this author had the main responsibility of both theoretical and experimental work, and prepared the manuscripts, supervised by Pertti Vainikainen. Xiongwen Zhao calculated the diffraction coefficient and helped in the measurements in [P5]. In [P6] this author had the main responsibility of both theoretical and experimental work and project management. The tapped delay line models (Section V) were mainly developed by Xiongwen Zhao. This author prepared the manuscript, except sections V A-C, and V F-G, which were originally written by Xiongwen Zhao. The work was supervised by Pertti Vainikainen. In [P7] this author upgraded the measurement system suitable for the campaign and gave consulting support during the measurements and the data analysis.

# 1 Introduction

Owing to the rapid increase in mobile radio communications, new frequency ranges and novel radio interface techniques will be employed in the near future [2]. In Europe, the third generation mobile systems are developed in the UMTS (Universal Mobile Telecommunications System) framework [3]. UMTS will operate at around 2 GHz frequency range. The fourth generation systems include the IEEE 802.11 standard at around 2.4, 5.3 and 5.8 GHz [4], the HIPERLAN (High Performance Local Area Network) standard at around 5.2, 5.6, and 17.2 GHz [4], and MBS (Mobile Broadband System) which is planned to operate at around 40 and 60 GHz [2] frequency ranges.

The services provided by future mobile radio networks, e.g. Internet and video transfer, require data rates substantially higher than those in use today. For example, capacity up to 54 Mbit/s has been specified for the IEEE 802.11 and HIPERLAN standards, and, at the 60 GHz frequency range, data rates as high as 155 Mbit/s have been proposed.

Due to the multipath propagation in the radio channel, the received signal is dispersed, which causes intersymbol interference (ISI). This limits the data rates of the techniques applied in the preceding generations of the mobile radio systems. Therefore, advanced wideband techniques will be employed in future radio networks. The next generation radio systems are intelligent; they adapt to the radio propagation environment by using advanced radio interface techniques, e.g. the Rake receiver in UMTS [3], OFDM (Orthogonal Frequency Division Multiplexing) [4] in HIPERLAN, and by adaptive antennas [5].

The design of the third and fourth generation systems and mobile networks requires modeling of the propagation environment, i.e. the radio propagation channel. Wideband radio channel models are empirical, semideterministic or deterministic. Empirical modeling is based on statistical analysis of a large number of measurements [6]. Deterministic modeling is based on electromagnetic simulation of the environment; the impulse response of the radio channel can be derived from the simplified environment by, for example finite difference time-domain (FDTD) method, or the ray-tracing approach, where dominant propagation paths are first predicted, e.g. [7] and [8]. Semideterministic modeling uses empirical modification of deterministic models.

Due to the complexity of the multipath propagation, reliable modeling requires measurements of the radio channel. A specific measurement device is needed for the radio channel measurements. The recorded channel can be used in the simulator, or empirical or semi-empirical models can be generated on the basis of measurement data [9]. Measurements can also be used for the study of the physical mechanisms of radio wave propagation- necessary to deterministic modeling.

## 1.1 Objectives of this study

This thesis aims to develop radio channel measurement techniques and radio channel characterization to meet the needs of future-generation radio systems.

## 1.2 Contents of the thesis

As part of this thesis, a direct sequence (DS) based wideband radio channel measurement system hardware i.e. a channel sounder was designed for microwave and millimeterwave (MMW) frequencies. The requirements for the sounding system, different measurement techniques, implementation questions (e.g., the effects of phase noise in radio channel measurements), and calibration strategy

for directional measurements were studied in [P1]–[P4]. The system was realized at 2.154 and 5.3 GHz, [P1], [P4], and [P7] and has been tested at 60 GHz. Measurements were performed at 5.3 GHz in both indoor and outdoor environments [P4]–[P7]. Indoor propagation mechanisms were studied by rotating a directive antenna in a channel sounder receiver [P5]. The indoor measurements were thoroughly analyzed, and empirical models were developed for wireless local area network system simulations [P6].

## 2    Wideband radio channel measurement techniques

### 2.1    Review of the measurement techniques for wideband radio channels

Radio channel characterization can be basically done with any transmitter-receiver configuration. Wideband measurement techniques have traditionally been divided by the used waveform into pulse and continuous-wave techniques[10], [11].

The main drawback of pulse sounding techniques (e.g.[12]) is that because the transmitted energy is pulsed they require a high power amplifier (PA) in the transmitter (TX), which increases the complexity of the system. Moreover, performing mobile measurements presumes licenses, which have power spectrum limitations of the transmitter.

Network analyzer is an obvious choice for wideband measurements [13]–[16]. The frequency sweeping waveform, which is rectangular in the frequency domain, has –13 dB sidelobes in the sinc-shaped delay-domain autocorrelation function. By using windowing functions to shape the signal, (e.g. [15]), trade-off between the sidelobe level and the mainlobe width can be applied. However, cable connection makes the network analyzer unpractical for large distances. In characterization of the radio channel, comprehensive measurement campaigns require a practical measurement device. The slowness of the frequency sweeping limits the Doppler range of measurement. Thus the measurement requires in practice a frozen environment. However, measurements campaigns with limited number of datasets have been performed even with virtual arrays (e.g.[17]) using optical antenna feed.

Direct sequence (DS) based methods, where phase-modulated pseudo-noise (PN) sequences are used as the sounding waveform, are nowadays widely used in radio channel characterization. Using the sliding correlator (SC) [18] principle, time/bandwidth scaling can be done in the receiver, which allows to perform wideband measurements with a relatively slow A/D conversion speed. Instead of a sliding correlator, a stepping correlator can be used, as in [19] and [20]. Today, A/D conversion can be done with several hundred megasamples per second, and direct sampling of the received signal [21] has advantages over the SC, especially in measurements with antenna arrays, which require rapid sampling of several antenna elements. The bottleneck in a system using rapid sampling is the speed of the bus between the sampling unit and the mass memory. In the DS-based channel sounder, energy is transmitted continuously. So, compared to the pulse method, less peak power equal to the effective operation time of the PA is required in the TX. The application of this method is presented in detail in this section.

The further development of DS based measurement techniques involves finding the optimal sounding waveforms with maximum spectral efficiency [22]. In this technique, combined with nonlinear predistortion, the rectangular spectrum shape is retained even after the RF power amplifier; hence the link budged is improved, and requirements for the TX-filters are relaxed.

## 2.2 HUT sounder

In this section, the sounder developed at Helsinki University of Technology partly as a part of this work is described. The sounder, which is based on the DS method, operates at 2.154 and 5.3 GHz center frequencies, and the extension to 60 GHz frequency range has already been tested.

### 2.2.1 Transmitter

In the transmitter (Fig. 2-1) the microwave carrier is modulated by the m-sequence generated in the PN generator. The PN generator consisting of feedback shift registers can generate $L$ = 31-2047 chip m-sequences. The chip rates $f_{chip}$ between 2.5 MHz − 30 MHz can be generated by a digital phase-locked loop (PLL). A double-balanced microwave mixer is used as a 2-PSK modulator. Mechanical realization is such, that the 2 and 5.3 GHz transmitters are separate units. Transmitted power is +40 dBm at 2 GHz with a separate power amplifier and +30 dBm at 5 GHz.
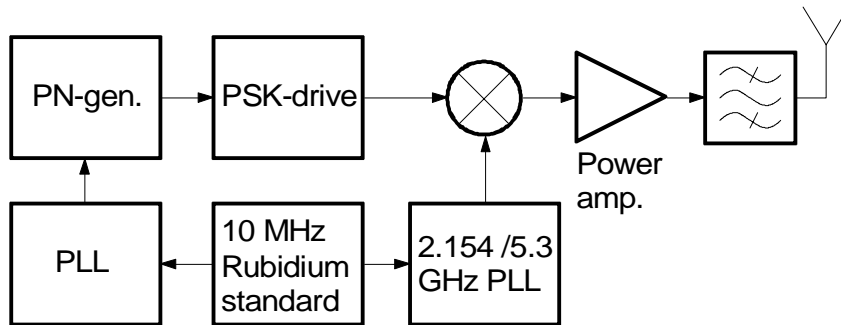


Fig. 2-1. Transmitter of the measurement system.

The chip rates higher than 30 MHz have a separate PLL and a code generator, which are realized using ECL-circuits. The maximum operating frequency of a code generator utilizing the linear feedback shift register is

$$\left(f_{chip}\right)_{\max} = \frac{1}{\tau_{SR} + n \cdot \tau_{gate} + \Sigma \tau_{tr} + \tau_{mux}}, \tag{2-1}$$

where $\tau_{SR}$, $\tau_{gate,}$ $\tau_{tr,}$ $\tau_{mux}$ are the shift register (SR) flip-flop, gate, transmission line, and multiplexer propagation delays (Fig. 2-2), respectively, and $n$ is the number of gates in series in the feedback loop having the longest delay.
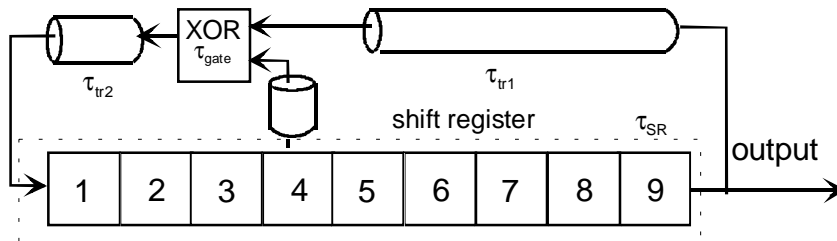


Fig. 2-2. Delays in the feedback shift register (the multiplexer to change the feedback paths is not shown).

Other topologies of high-speed code generators can be realized using e.g. FPGAs. Chip rates higher than 1 GHz have been realized [23]. The performance of the DS channel sounder is evaluated on the basis of waveform autocorrelation properties. The autocorrelation $R_s(\tau)$ of the periodic signal $s(t)$ with period $T_s$ is defined as

$$R_s(\tau) = \frac{1}{T_s} \int_0^{T_s} s(t)s^*(t-\tau)dt .$$ (2-2)

The autocorrelation of the waveform is related to the power spectrum $S_p(f)$ of the signal by the Wiener-Kinchine-relation and hence to the Fourier transform of the signal $S(f)$ by (e.g. [24] )

$$R_s(\tau) = \mathcal{F}^{-1}(S_p(f)) = \mathcal{F}^{-1}(S(f) \cdot S^*(f)).$$ (2-3)

Autocorrelation of the high-speed code generator output waveform with $f_{chip} = 166.7$ MHz is shown in Fig. 2-3. The waveform was sampled with a digital oscilloscope, and the autocorrelation was calculated off-line by (2-3). The envelope of the spectrum of a signal with 53.75 MHz chip rate upconverted to 5.3 GHz is shown in Fig. 2-4. Because the signal is periodic, the spectrum is a line spectrum, where the lines are separated by $f_{chip}/L$. This is not seen in Fig. 2-4 due to the limited resolution of the spectrum analyzer. In the radio channel measurements, filters must be applied in TX, because the sidelobes of the spectrum are not allowed by the transmission regulations. Furthermore, the sidelobes reduce the power efficiency of the measurement. Moreover, signal components that remain outside of the information bandwidth of the A/D converter are aliased, and increase the noise level in the measurement process.
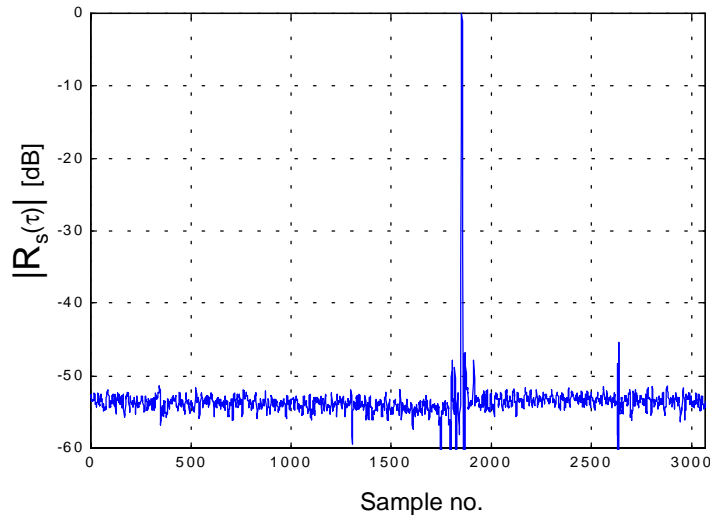


Fig. 2-3. Autocorrelation of a PN code waveform, $f_{chip} = 166.7$ MHz, sampling rate is 1 GHz, $L = 511$ (realized with two ECL-ICs). Spurious level is -45 dB.
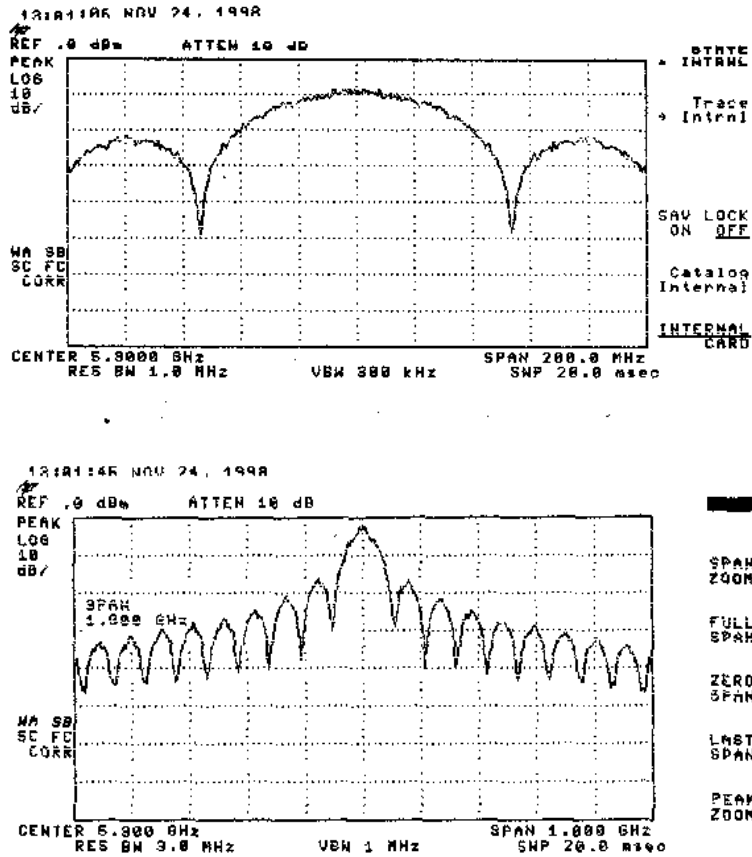
Fig. 2-4. Output power spectrum of the transmitter without filters at 5.3 GHz, $f_{chip}$ = 53.75 MHz, $L$ = 511.

### 2.2.2 Receiver

In the receiver (Fig. 2-5) RF front-end, the antenna signal is filtered ($B$ = 100 MHz), amplified in a low-noise preamplifier and downconverted to 300 MHz intermediate frequency (IF) with the total single-sideband noise figure of 2.5 dB. The IF-stage includes automatic gain control (AGC) with computer-controlled digital step attenuators having a dynamic range of 72 dB, and a major part of the signal amplification. The 2 and 5 GHz versions are realized with two interchangeable plug-in units. The major improvement to the system that is not included in [P1] is the separate sampling unit for inphase (I) and quadrature (Q) channels. Also, microwave switch arrays in front of the RF-front end to measure antenna arrays with two polarizations have been realized [25].
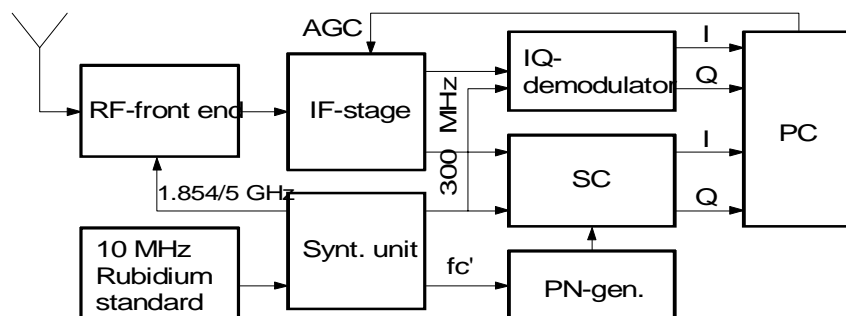


Fig. 2-5. The receiver block diagram.

### 2.2.2.1 Matched filtering

In [P1], basic limitations of the sounder concept are discussed. In this work, the post processing with super resolution algorithms is not covered. It is assumed that a matched filter (MF), realized either by digital signal processing (DSP) or by SC, is used as a detector. The impulse response of the matched filter $h_{MF}$ is the mirror image of the signal waveform in the time domain

$$h_{MF}(\tau) = s(-\tau). \tag{2-4}$$

In the frequency domain, (2-4) can be written using the corresponding Fourier transforms

$$H_{MF}(f) = S^*(f). \tag{2-5}$$

The impulse response of the radio channel is estimated from the received complex signal $r(t)$ by

$$\hat{h}(\tau,t) = h_{MF} \otimes r(t). \tag{2-6}$$

Using the frequency domain notation, (2-6) can be written as

$$\hat{h}(\tau,t) = \mathcal{F}^{-1}\big(R(f) \cdot S^*(f)\big), \tag{2-7}$$

where $R(f)$ is the Fourier transform of the received signal over the time of the signal period. This implies, that the IR estimation is averaged over the period of the measurement waveform. In [P1], the use of deconvolution as enhancement of delay resolution is discussed. Then IR is estimated by

$$\hat{h}(\tau,t) = \mathcal{F}^{-1}\left(\frac{R(f) \cdot S^*(f)}{S_p(f) + \gamma}\right), \tag{2-8}$$

where $\gamma$ adjusts the trade-off between resolution and dynamic range.

### 2.2.2.2 Bandwidth limitation

The RF parts of the measurement system, described by their impulse response $h_{sys}$ in [P1] affect the signal autocorrelation and hence the dynamic range and the resolution of the system. The impulse responses of the band limiting filters of the system mainly contribute to $h_{sys}$. As demonstrated in [P1], filters with sharp cutoff have high transient response (e.g. [26]). Filters must be applied to reject the sidelobes of the sinc-spectrum in the TX (Section 2.2.1), and the interference, image frequency and spurious signals in the RX, and to prevent the aliasing of noise and interference to the information band in the sampling process. To reduce the transient responses, the phase distortion of the filters can be compensated in off-line processing by multiplying the received signal $R(f)$ with the complex conjugate of the baseband transfer function of the filter $H_f(f)$

$$\hat{h}(t,\tau) = \mathcal{F}^{-1}\big(R(f) \cdot S^*(f) \cdot H_f(f)^*\big). \tag{2-9}$$

Filter effects can be further reduced by deconvolution [27], which requires high SNR. Obviously, linear phase filters are preferable in channel sounding applications, since they do not cause transient

responses [26]. In the filter design procedure, Bessel polynoms approximate such filter. However, conversion from baseband prototype to band-pass filter does not completely preserve the linear phase characteristics [26]. In Figures 2-6 and 2-7, the system response of the 5 GHz version of the sounder is presented, measured with $L = 511$, $f_{chip} = 60$ MHz, and sampling rate is twice the chip rate. The narrowest filter is the anti-aliasing filter at baseband, which is a 5-stage Bessel filter with the 3 dB bandwidth of 35 MHz. Filter requirements especially in the TX can be relaxed by applying waveforms described in [28] and [22]  -instead of the conventional m-sequence generator an off-line optimized  waveform with rectangular spectrum is generated from digital memory.
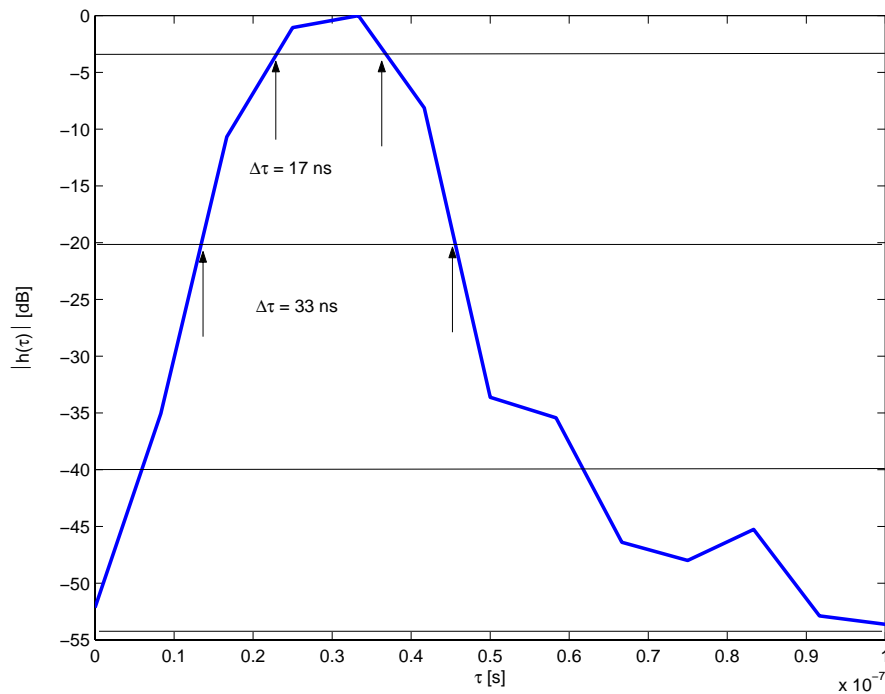


Fig. 2-6. The mainlobe of the measurement system response.
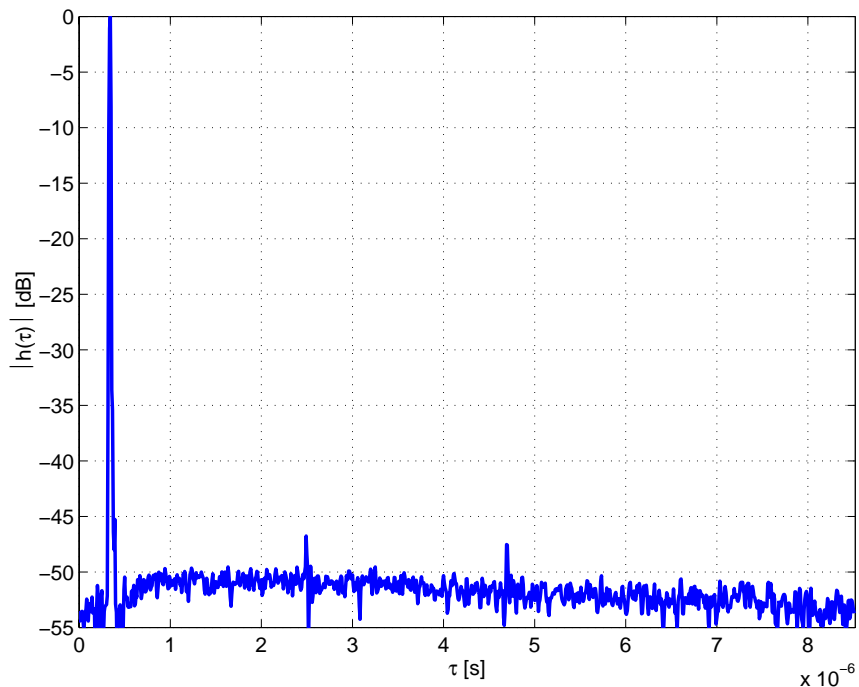


Fig. 2-7. The measurement system response.

14

### 2.2.2.3 Sliding correlator

In the SC, a replica of the transmitted m-sequence is generated in the receiver with a chip rate $f_{chip}'$. The scaling factor $K$ is defined by the difference of the TX and RX chip rates:

$$K = \frac{f_{chip}}{f_{chip} - f_{chip}'} .$$  (2-10)

The RX sequence is upconverted to the IF and correlated with the received signal in an analog correlator, which consists of double-balanced mixers and integrators for I and Q channels [1]. The complex output of the SC $r'(t)$ is the convolution of the IR $h(\tau,t)$ and the crosscorrelation $R'_s(\tau)$ of the TX and RX baseband signals

$$r'(t) = h(\tau,t) \otimes R_s'(\tau),$$  (2-11)

where $\tau$ is a function of time: $\tau = t \cdot K$ and '$\otimes$' denotes convolution. Bandwidth compression by the amount of $K$ is achieved at the cost of the measurement time. Thus $f_{Dmax}$ is limited to a few tens of Hz at maximum. However, in an analog correlator, the delay range can be zoomed by resetting or shifting the reference m-sequence generator. Thus, Doppler range can be enhanced to hundreds of Hz.

Response of the system with parameters $f_{chip} = 53.75$ MHz, $L = 511$ and $K = 2150$ is shown in the Fig. 2-8. The I and Q time/bandwidth scaled IR components are A/D-converted to 12 bits with maximum $2 \cdot 500$ kHz sampling rate. The data can be stored in real time to the mass memory of the PC. Thus the length of the measurement route is not limited in practice.
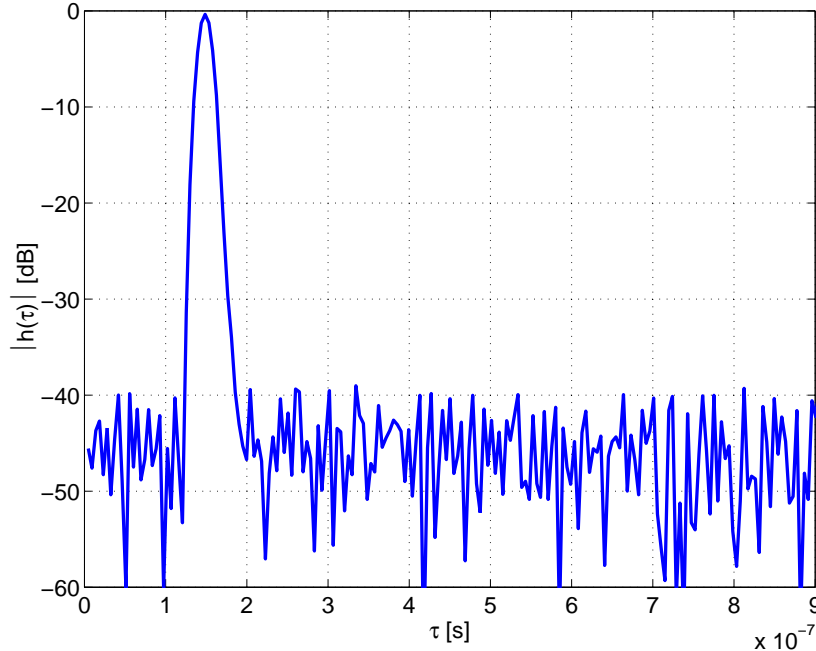


Fig. 2-8. Response of the measurement system using SC, $f_{chip} = 53.75$ MHz, $K = 2150$, $L = 511$.

### 2.2.2.4 Data acquisition

The requirements of high speed sampling and data storage can be avoided by using the SC, where the bandwidth is scaled down by $K$. The SC was applied in this work in publications [P4], [P5] and [P6], which included indoor measurements. However, measurements with the switched antenna ar-

15

rays and switched polarizations cannot be performed with time/bandwidth scaling with a reasonable vehicle speed. Moreover, performing the A/D conversion before the correlation avoids the nonidealities of the analog correlator, e.g. the noise caused by the difference of the chip rates in RX and TX.

In high-speed sampling of the signal, the bottleneck in the setup described in [P1] was the limited amount of on-board memory of the sampling board. The measurements described in [P7] were performed in 30 m stretches. So the data was discontinuous, and the measurement procedure was tedious. After this campaign, an external sampling was purchased. So the data rate of 2·20 Ms/s can be stored with the external 9 GB hard disks of the measurement system. The complexity of high performance data acquisition increases the cost, size, weight, and power consumption of the receiver.

The complex impulse response can be sampled with a single sampling board by direct IF-sampling (e.g. [21]). In this work, a sampling scheme depicted in Fig. 2-9 was experimented. The center IF is 300 MHz, and the information band is 200 MHz–400 MHz. When the sampling rate is 400 MHz, the information aliases to DC–200 MHz. The I and Q components of the signal can be separated in off-line-processing. In section 2.2.2.2, a sampling rate of two samples/chip was sufficient with a proper anti-aliasing filter. In the scheme of Fig. 2-9, the corresponding sampling rate is four samples/chip. Thus, a chip rate of 100 MHz can be used with the scheme.
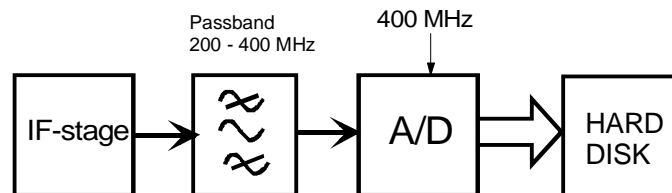


Fig. 2-9. Block diagram of direct IF-sampling.

## 2.3    Extension to 60 GHz

In this work, extension of the sounder concept to millimeter waves (MMW) was designed, associated with Ylinen Electronics and the Electronic Circuit Design Laboratory of HUT. At the moment of publication of this thesis, the extension has been partly tested. The principle is to use the 5.3 GHz version of the sounder with up conversion to 60 GHz frequency range in the TX. In RX, the measurement signal is down converted to 5.3 GHz. The main operation frequency range of this setup is in the industrial, scientific and medical (ISM) band, with center frequency at 61.22 GHz.

The MMW-units (Fig. 2-10, 2-11) consist of phase-locked oscillators (PLO) with multiplier chains (described in Section 2.4.1), mixers, image frequency rejection filters (waveguide high-pass) and a power amplifier in TX and a low-noise amplifier in RX. The PLOs of the system are phase-locked to the 10 MHz primary standard of the system. The balanced mixers are realized with fin-line technology. The image frequency rejection filter is a narrowed WR-15 waveguide with a cut-off frequency of 58 GHz. The amplifiers are realized with GaAs MMIC-technology. The GaAs power amplifier has a 1 dB compression point of +15 dBm measured on wafer [29]. The noise figure of the LNA is 4.5 dB [29]. The omnidirectional antennas are biconical horn antennas [30] operating in the WR-15 frequency range. The measured gain of the antennas is about 5 dB. The low noise frequency synthesis is described in the following section. The impulse response of a back-to-back measurement shown in Fig. 2-12 was obtained without the MMW amplifiers, and using laboratory synthesizers having higher phase noise than the final design as local oscillators.
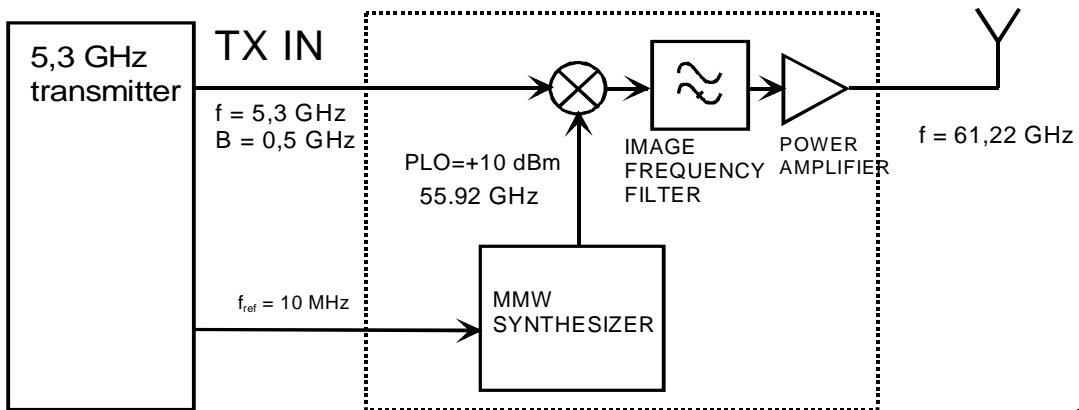
Fig. 2-10. The transmitter of the measurement system
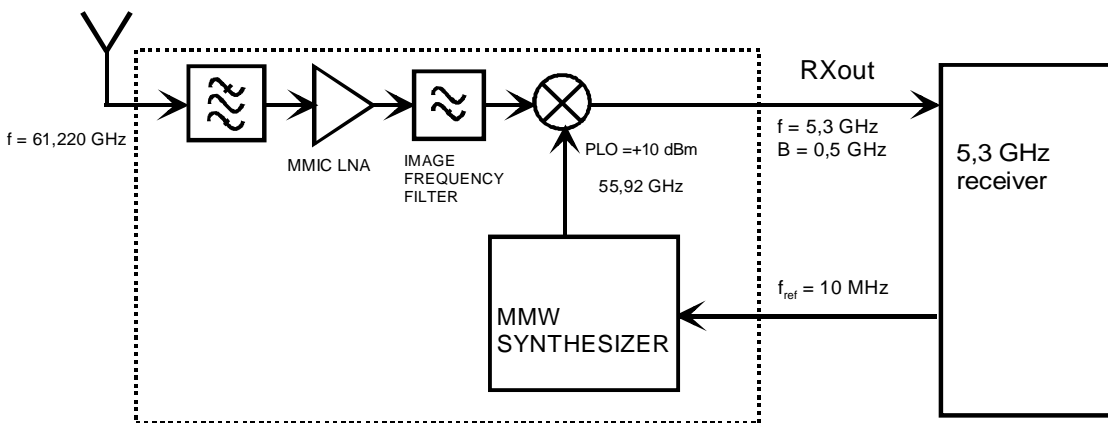


Fig. 2-11. The receiver of the measurement system.
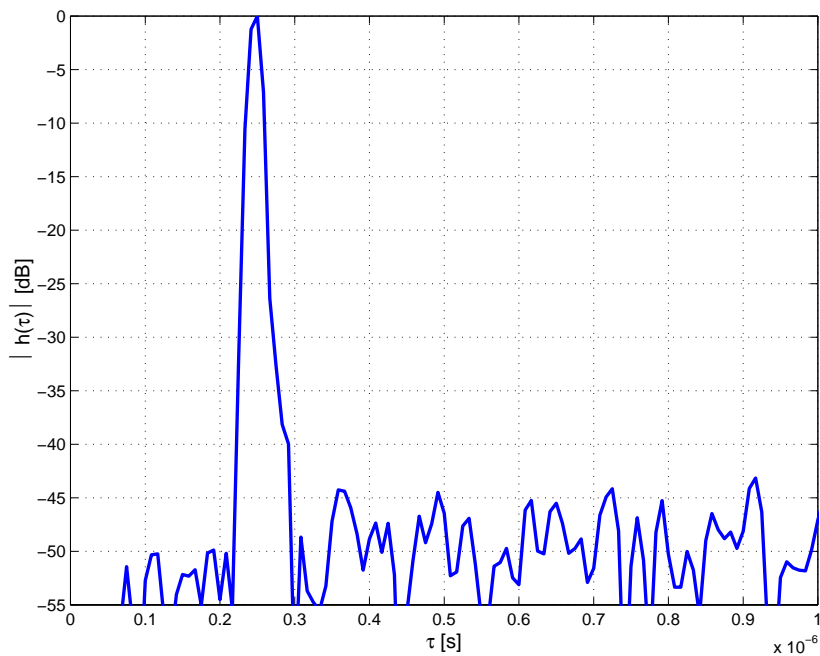


Fig. 2-12. Result of a back-to-back measurement of the MMW test setup using laboratory synthesizers, $L = 511$, $f_{chip} = 60$ MHz.

## 2.4 Low noise frequency generation

In [P1]–[P3], the effects of the phase noise in the radio channel measurements are discussed. Minimizing the phase noise is required especially in measurements at MMW frequencies. This can be done by applying a dielectric resonator oscillator (DRO) and a multiplier chain as a local oscillator, giving superior performance compared to the phase locked Gunn oscillator, analyzed in [P2]. Phase noise requirements will be discussed in Section 2.7 .

### 2.4.1 Low noise PLL topology

A simplified expression for the power spectral density of phase fluctuations of the synthesizer of Fig. 2-13 can be presented according to [31] as

$$S_\phi(f_b) = \left( \left[ S_{\phi ref}(f_b) + S_{\phi PD}(f_b) \right] \cdot \left| H(j2\pi f_b) \right|^2 \cdot N_1^2 + S_{\phi VCO}(f_b) \cdot \left| 1 - H(j2\pi f_b) \right|^2 \right) \cdot M_2^2, \qquad (2\text{-}12)$$

where $S_{\phi ref}$ denotes the primary standard, $S_{\phi PD}$ the phase detector and $S_{\phi VCO}$ the voltage controlled oscillator (VCO) noises, $N_1$ ( = 466) is the ratio of the VCO output frequency and the primary standard frequency, $M_2$ (= 12) is the total multiplication of the multiplier chain after the VCO, and $H(j2\pi f_b)$ is the effective transfer function of the PLL. The phase detector SSB noise is estimated to be -140 dBc, and the noise of the VCO is estimated from [32]. The contributions of the different noise sources and the resulting noise are shown in Fig. 2-14. Inside of the PLL bandwidth the noise of the primary standard dominates. Outside of the PLL bandwidth ($H \approx 0$) the noise of the VCO dominates.
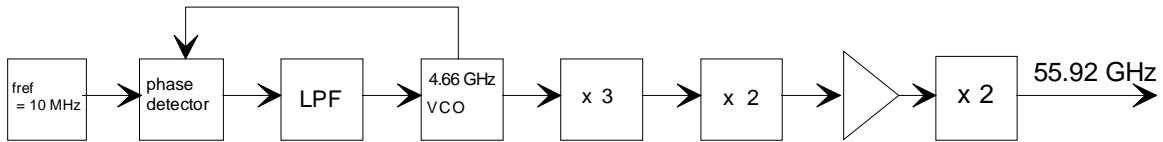


Fig. 2-13. Block diagram of the millimeter wave phase-locked oscillator (LPF = low pass filter).
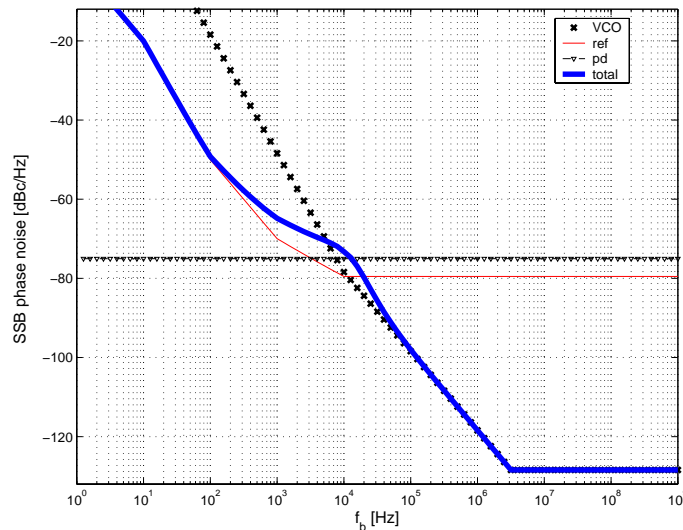


Fig. 2-14. Contributions of the different components to the spectral density of phase noise.

### 2.4.2 Noise of the primary standard

Noise of the primary rubidium standard near the carrier can be described by the Allan variance, i.e., the variance between adjacent frequency samples

$$\sigma_y^2(\tau) = \frac{\left\langle \left(\bar{y}_{l+1} - \bar{y}_l\right)^2 \right\rangle}{2}, \tag{2-13}$$

where $\bar{y}_l$ is the fractional frequency fluctuation averaged over a sample time $\tau$ [33]. Typical noise characteristics of a rubidium standard are shown in Fig. 2-15 [34]. Different slopes are due to the different dominating noise processes in oscillators; these are white phase noise due to the thermal noise, flicker phase noise, white frequency noise, flicker frequency noise, and random-walk frequency noise. The correspondence between the slopes of spectral density of phase fluctuation $n$, spectral density of frequency fluctuation $\alpha = n+2$, and $\sigma_y(\tau)^2$ with the different processes are explained in e.g. [35].
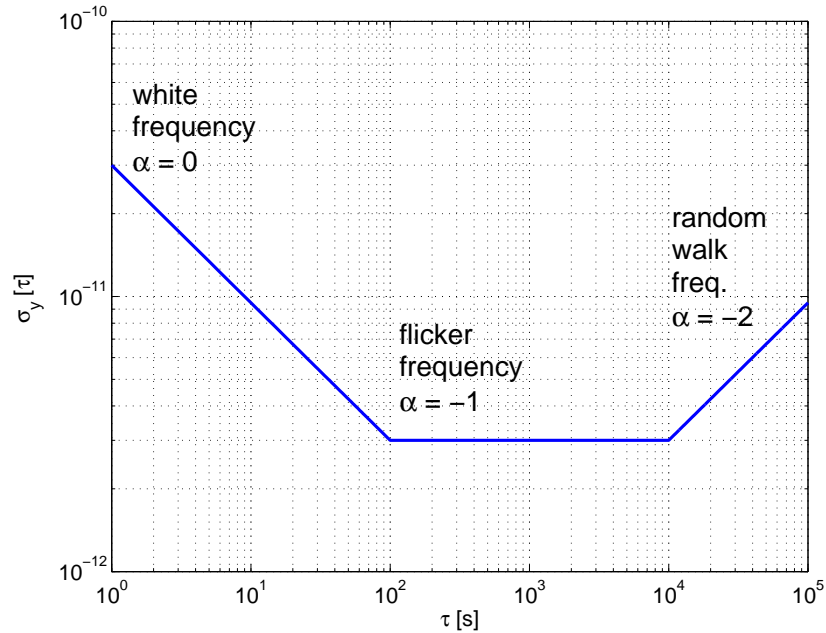


Fig. 2-15. Typical stability of a rubidium standard [34].

## 2.5 Direction of arrival estimation techniques.

In [36], direction of arrival estimation techniques are divided into
1. High-gain directional antenna,
2. Synthetic aperture and beam forming methods,
3. High-resolution algorithms.

In this work, method 1 was used in [P5]. Although the antenna gain was only 13 dBi, sufficient information was obtained to determine the main propagation paths in 2 dimensions. In [37], virtual cross array was experimented. High-resolution algorithms (e.g. ESPIRIT [38] and SAGE [39]) are beyond the scope of this work.

### 2.5.1 Setup with a rotating antenna

Due to the mechanical rotation, the setup with a rotating antenna is inherently slow, and requires a frozen environment. A three-dimensional measurement needs in practice rotation around two axes (e.g.[40]). In [P5], the TX antenna was an omnidirectional vertical polarization discone antenna. The receiver antenna was a pyramidal horn antenna, which was rotated 360° with an antenna rotator. The SC configuration (Section 2.2.2.3) of the sounder was used. The sampling interval was 0.44°.

The 3 dB beamwidth of the horn antenna was 30° in the H-plane and 37° in the E-plane. The peak sidelobe level was 26 dB. The beamwidth in the H-plane gives the azimuth angular resolution of the measurement. In Fig. 2-16, an example of a measured set of IRs with 20 dB dynamic range relative to the strongest propagation path is shown. The figure presents a non line of sight (NLOS) case.
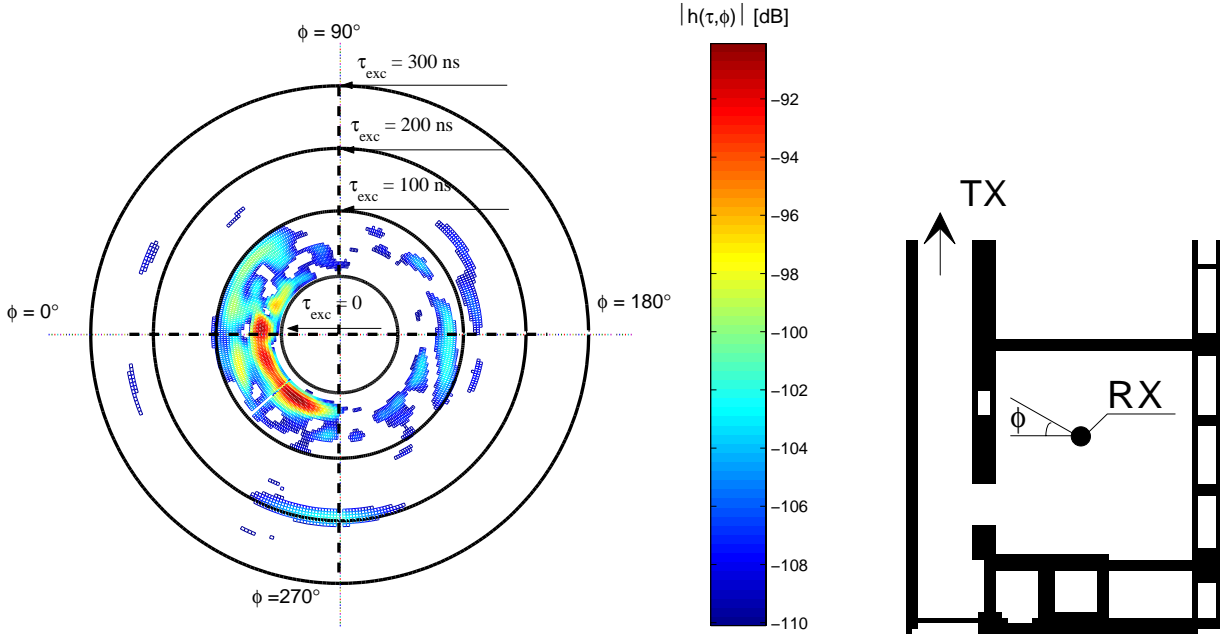


Fig. 2-16. DOA estimation using rotating directive antenna. The distance between RX and TX is about 27 meters.

### 2.5.2 Setup with a virtual array

DOA from an arbitrary antenna array with $n_A$ elements can be resolved from the phase difference of the signal in the different array elements. The IR with an angle of arrival in the azimuth $\phi$ and elevation $\theta$ angle can be calculated by Fourier-processing

$$\hat{h}(\tau,t,\phi,\theta) = \sum_{n=1}^{n_A} \hat{h}(\tau,t,n) \cdot v_s(\phi,\theta,n), \qquad (2\text{-}14)$$

where $v_s(\phi,\theta,n)$ is the steering matrix of the array, which can be derived from the array geometry. Simplest array is the linear array, where $\theta$ is ambiguous (e.g. [25]). By placing elements in two dimensions like in a cross array shown in Fig. 2-17 [37], [41], the ambiguity is partly resolved. However, the upper and the lower hemisphere are still ambiguous, so third dimension in the array geometry is preferable, see e.g. [16]. Arrays with circular [13], [20], [42] and spherical [43] shape have also been used in radio channel measurements. When the measurement is slow, phase noise has to be taken into account, if RX and TX are not connected with a cable (Section 2.7.2). A virtual array can be made large [44], so high resolution can be obtained. However, the far-field condition must apply considering the largest dimension of the array. Otherwise, the convexity of the wavefront causes that the radiation source seems to be spread in space, when the plane-wave approximation is used in DOA estimation. When a single antenna is moved to form the virtual array, a frozen environment is required. Dynamic measurements with different switched arrays can be performed using an RF-multiplexer, as in [25], [43], and [44]. In [44], the RF-multiplexing and mechanical positioning were combined.
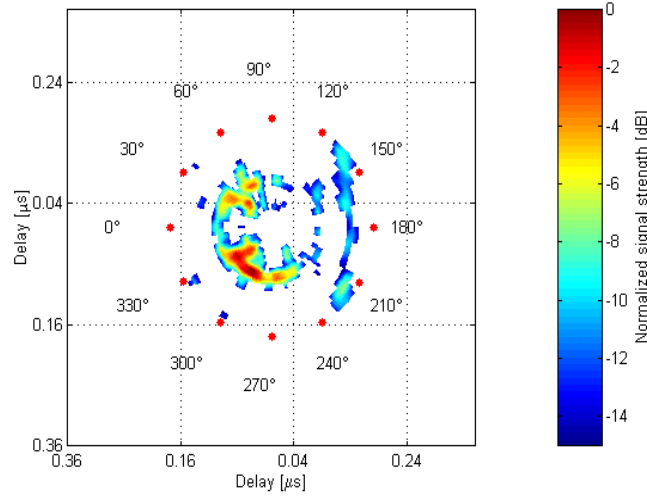
Fig. 2-17. DOA estimation using a cross array [37].

## 2.6 Link budget evaluation

In this subsection, the link budget is derived as a function of the dynamic range requirement. The detection is performed using MF. Nonidealities of the SC are also considered.

### 2.6.1 Noise floor of the waveform autocorrelation

The noise floor in the autocorrelation of an ideal m-sequence is (in voltage)

$$D_{code} = -\frac{1}{L}. \tag{2-15}$$

In a real measurement, the dynamic range is affected by the multipath propagation in the radio channel. The noise floor sums from all the paths that can be resolved by the MF

$$D_{code} = -\frac{1}{L} \cdot \sum_{k=1}^{N_p} a_k \cdot e^{j \cdot \gamma_k}. \tag{2-16}$$

In the worst case, $D_{code}$ increases proportionally to the number of paths $N_p$ [P1]. In a general case with high number of paths, when $a_k$ has normal distribution and $\gamma$ uniform distribution between [0, 2 $\pi$], $D_{code}$ has Rayleigh distribution with the mean value (e.g.[24] )

$$\overline{D}_{code} = -\frac{1}{L} \cdot \sqrt{\frac{N_p \cdot \pi}{4}}, \tag{2-17}$$

so $|D_{code}|$ increases proportionally to $\sqrt{N_p}$ .

### 2.6.2 Spurious peaks in the waveform autocorrelation

Spurious peaks in the autocorrelation are caused by the nonidealidies of the code generator and the 2-PSK modulator. In the following, the spurious peaks are neglected in the calculations of the dynamic range and the link budged; $D_{code}$ refers to the average level of the noise floor. However, the

21

dynamic range $D$ cannot be higher than the relative spurious level of the measurement system response, which is –47 dB below the strongest signal in Fig. 2-7 and –30 dB in the setup described in [P7].

### 2.6.3  Requirement of signal-to-noise ratio in the input of the MF

Detection of the IR using MF and averaging is described in Fig. 2-18. The signal and noise amplitudes in the output of this block are

$$v_{sout} = L \cdot N_{ave} \cdot v_{sin} \tag{2-18}$$

$$v_{nout} = \sqrt{L \cdot N_{ave}} \cdot v_{nin} \tag{2-19}$$

Hence the signal-to-noise ratio in voltage improves by $\sqrt{L \cdot N_{ave}}$ .
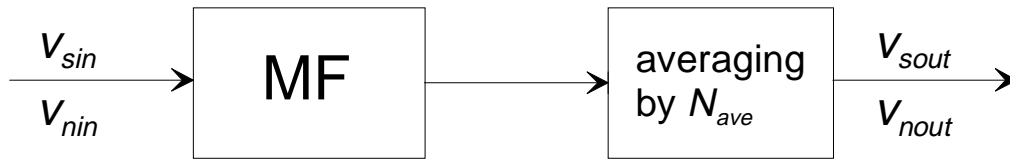


Fig. 2-18. Matched filtering and averaging.

The white noise is uncorrelated with the PN-code. So the dynamic range (in voltage) of the measurement in the presence of Gaussian noise can be presented as

$$D = \frac{1}{\sqrt{D_{code}^2 + \dfrac{x^2}{L \cdot N_{ave} \cdot SNR_v^2}}} \,, \tag{2-20}$$

where $x$ presents the noise amplitude normalized with respect to the rms value $\left| v_n \right|$ .

$$x = \frac{\left| v_x \right|}{\left| v_n \right|}. \tag{2-21}$$

The probability that noise is detected as a propagation path is then

$$P_e = 2 \cdot Q(x), \tag{2-22}$$

where $Q$ is the CDF of the tail of the Gaussian distribution. Typical requirement for $P_e$ is 0.002, which corresponds to $x = 3$. The requirement for the SNR in dB can be written as

$$SNR[\text{dB}] = 10 \log \left[ \frac{x^2}{L \cdot N_{ave} \cdot \left( \dfrac{1}{D^2} - D_{code}^2 \right)} \right]. \tag{2-23}$$

When $L \gg D$, this equation simplifies to

$$SNR[\text{dB}] = D[\text{dB}] - 10 \log(L \cdot N_{ave}) + 20 \log(x) . \tag{2-24}$$

### 2.6.4 Nonideality of sliding correlator

In SC, lagging of the TX and RX codes produces distortion, which increases in voltage proportional to $\sqrt{L/K}$ and is decreased in the correlation process proportional to $\sqrt{K}$. Distortion from different paths sums independently. So (2-20) is modified on semi-empirical basis (L > K)

$$D = \frac{1}{\sqrt{D_{code}^2 + \dfrac{L \cdot N_p}{K^2} + \dfrac{x^2}{K \cdot SNR_v^2}}}. \qquad (2\text{-}25)$$

Compared with simulations in [46], (2-25) is slightly optimistic. The code lag causes detection loss in the MF process, which increases both the second and third term of the denominator in (2-25). This is significant, when $K/L \sim 1$.

### 2.6.5 Requirement for the input power in the receiver

The requirement for the input power of the receiver is

$$P_{in}[\text{dBm}] = P_n[\text{dBm}] + SNR[\text{dB}], \qquad (2\text{-}26)$$

where $P_n$ includes the receiver noise reduced to the antenna output and antenna noise. The maximum measurable path loss (including antenna gains) is

$$PL_{\max}[\text{dB}] = P_{TX}[\text{dBm}] - P_{in}[\text{dBm}]. \qquad (2\text{-}27)$$

### 2.6.6 Cramér-Rao lower bound in delay domain

The arrival time of a signal component can be determined with enhanced precision by applying maximum likelihood estimation in the data post processing. This can be done after the matched filtering by the analog or digital correlator. The ultimate limit for the unbiased precision of the arrival time is given by the Cramer-Rao lower bound (CRLB)

$$Var(\hat{\tau} - \tau) \geq \frac{1}{2 \cdot \dfrac{E_r}{N_0} \cdot \beta^2}, \qquad (2\text{-}28)$$

where $E_r/N_0$ is the signal-to noise ratio in power in the output of the matched filter and $\beta$ is the signal radian bandwidth at baseband, i.e. the second central moment of signal spectrum around $f = 0$ ([47], p. 411). It follows from (2-28), that if the measurement signal is uniformly spread over the information bandwidth, the minimum variance improves along with the bandwidth with constant energy $E_r$. Another implication of (2-28) is that the optimum waveform to have the highest precision is rectangular in the frequency domain, as was also noted in [28]. Applying the mainlobe of the sinc-spectrum to (2-28), CRLB for the setup described in [P1] is of the order of 1 ns, when $E_r/N_0$ is about 20 dB.

## 2.7 Effect of phase noise

### 2.7.1 Effect on dynamic range

The result of [P5] for the dynamic range of the measurement can be combined with (2-20), assuming that the phase noise rms value $\phi_{rms}$ is small and $N_{ave} = 1$

$$D = \frac{1}{\sqrt{D_{code}^2 + \dfrac{x^2}{L \cdot SNR_v^2} + \dfrac{x^2 \cdot \phi_{rms}^2}{L}}} \, . \tag{2-29}$$

For example, assuming $x = 3$ and $L = 511$, and $N_p = 1$, the dynamic range vs. SNR with phase noise values from $0°$ to $10°$ is shown in Fig. 2-19.

Obviously, the frequency synthesizer with the highest output frequency has the most significant contribution to the phase noise of the system. We also assume that the RX and TX synthesizer noises are equal and independent. Then $\phi_{rms}$ can be estimated from the phase noise SSB spectral density $\mathcal{L}(f_b)$ as in [48]

$$\phi_{rms} = 2 \cdot \int_{f_1}^{f_2} \mathcal{L}(f_b) df_b \, . \tag{2-30}$$

where $f_1$ is the reciprocal of the sampling time of an IR and $f_2$ equals the baseband bandwidth.

It can be seen, that small values of phase noise cause detection loss, when requirements for dynamic range are high. Excessive values of phase noise cause an irreducible noise floor, which is given by the third term of (2.29). Phase noise is a problem especially at 60 GHz frequency range where the phase noise is highest, and the TX power is also limited to about 16 dBm due to amplifier technology. So the detection loss cannot be tolerated. Because the size and cost of the frequency synthesizer are not critical in low microwave frequencies, phase noise is negligible, provided that proper phase-locked oscillator designs are used.
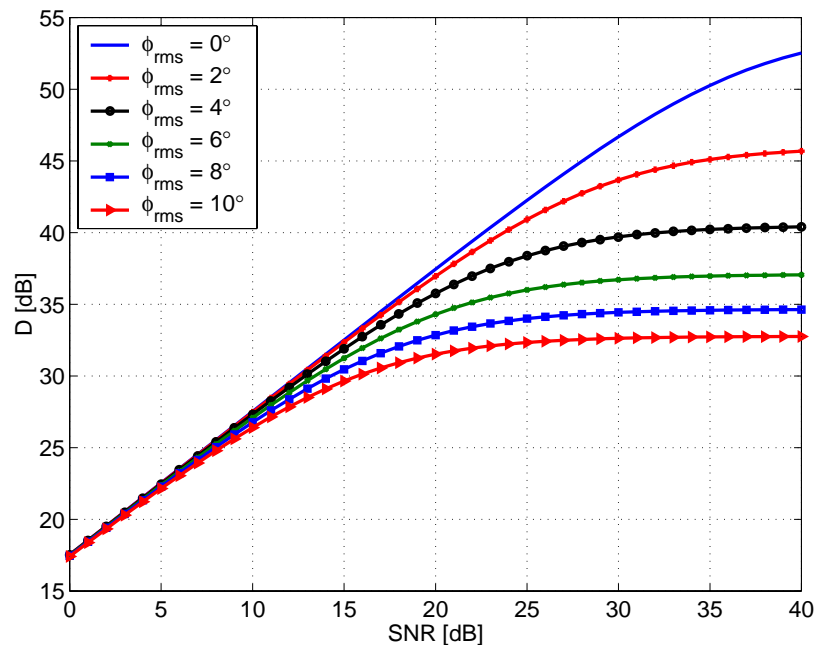


Fig. 2-19. Dynamic range vs. SNR with different rms phase noise values ($L = 511$).

## 2.7.2 Effect on DOA estimation

It is shown in [P3] that the minimum standard deviation in direction of arrival estimation in a bistatic measurement without cable connection between TX and RX in a switched or virtual linear array is

$$\sigma_{DOAE}(T_e, n_A) = 2 \cdot f_c \cdot T_e \cdot \sigma_y((n_A - 1) \cdot T_e), \qquad (2\text{-}31)$$

where $T_e$ is the time interval between measurements of consecutive elements, $n_A$ the number of elements and $f_c$ the carrier frequency. The factor 2 equals the number of measurement points per wavelength. The Allan variance is calculated from the spectral density of fractional frequency fluctuations $S_y(f_b)$ [33]

$$\sigma_y{}^2(\tau) = 2 \cdot \int_0^\infty S_y(f_b) \cdot \frac{\sin^4(\pi f_b \tau)}{(\pi f_b \tau)^2} df_b, \qquad (2\text{-}32)$$

Equation (2-31) assumes that each measurement is calibrated separately by scanning the antenna in opposite directions. Thus the corresponding DOA estimates (i. e. scatterer profiles) are shifted, and the frequency offset can be estimated. The effect of deadtime from the calibration is taken into account by

$$\sigma_{DOAE}(T_d, T_e, n_A) \approx \sqrt{3} \cdot \sqrt{B_2(T_d, T_m)} \cdot \sigma_{DOAE}(T_e, n_A), \qquad (2\text{-}33)$$

where $B_2(T_d, T_m)$ is the bias function caused by the deadtime [P3], i.e. the ratio of the average variance with deadtime between measurements to that of no deadtime. In [P3], the analysis done for the 5 GHz version of the sounding system is shown. The errors are of the order of a fraction of degree with a switched array. For virtual arrays, which require element measurement times of the order of milliseconds, the speed of the measurement is essential; in the typical "white noise FM" region the $\sigma_{DOAE}$ increases along with the square root of $T_e$.

## 3 Propagation in indoor environments

Modeling radio wave propagation requires studying propagation mechanisms. It is not expected in near future, that a radio wave propagation simulation software could calculate the field from Maxwell's equations. Rather, calculation is simplified like in the ray-tracing approach, or based on semi-empirical models. Therefore, it is important to study, which propagation mechanisms are significant. In this work, propagation mechanisms at 5.3 GHz were studied on the basis of theoretical calculations and by rotating a directive antenna in [P5]. This measurement method was selected because it gives unambiguous results with high dynamic range.

Statistical models were developed using data measured with mainly omnidirectional antennas [P6]. Statistical modeling allows unlimited number of simulations with random processes, compared to recorded channel, which allows only limited number of simulations due to the limited number of measurements.

## 3.1 Propagation mechanisms

### 3.1.1 Propagation in free space

The free space pathloss with wavelength $\lambda$ at distance $d_0$ in the far-field of the antennas with gains $G_1$ and $G_2$ is given by

$$PL_0\left(d_0\right) = -G_1 - G_2 + 20 \cdot \log\left(\frac{4\pi d_0}{\lambda}\right). \tag{3-1}$$

Equation (3-1) can be used for separate rays, when the first Fresnel zone is free from obstructions [49].

### 3.1.2 Ray theory

In the ray theory, it is approximated that the energy propagates between antennas inside ellipsoid shaped tubes, defined by the first Fresnel zone [49]. The phase difference between the straight line and the line via the equivalent source on the surface of the tube is 180°. According to the theory, only obstacles inside the tube may affect on the energy. At 5.3 GHz, the maximum diameter of the tube is 1 meter when the length of the ray is 18 m. The ray theory was used in [P5] to distinguish separate rays to study the mechanisms associated with each ray.

### 3.1.3 Refraction, reflection and transmission in the boundary of dielectric media

In the following equations, we assume that the wave can be regarded as a plane wave. So the field in point $r$ is given by

$$E\left(r\right) = E_0 \cdot e^{-j\mathbf{k} \cdot \mathbf{r}}, \tag{3-2}$$

where $\mathbf{k}$ is the wave vector. The boundaries are assumed smooth compared to wavelength, and uniform inside the first Fresnel zone.

#### 3.1.3.1 Refraction

The energy can propagate behind wedge-like obstacles, through both refraction and diffraction. It can be easily calculated from Snell's law that refraction behind 90° corners requires $\varepsilon_r < 2$. Such wedges where refraction can be a dominant propagation mechanism seldom exist in indoor environment, so refraction can be neglected when dominant propagation mechanisms are discussed.

#### 3.1.3.2 Reflection

The dielectric medium has relative dielectric permittivity $\varepsilon_r = \varepsilon_r' - j\varepsilon_r''$. Fresnel reflection coefficients $r_\perp$ and $r_\parallel$ for perpendicular and parallel polarizations, respectively, for a plane wave in the boundary of dielectric media are well known, e.g.[49].

#### 3.1.3.3 Transmission

For a layer with thickness $d$ of homogeneous dielectric medium the field transmission coefficient is (e.g. [50])

$$T = \frac{(1-r^2)\cdot e^{-j\delta}}{1-r^2 e^{-j2\delta}}, \tag{3-3}$$

where $r$ can be either parallel or perpendicular field reflection coefficient, and

$$\delta = \frac{2\pi d(\sqrt{\varepsilon_r})}{\lambda \cdot \cos\phi_2}, \tag{3-4}$$

where $\phi_2$ is the direction of propagation inside the dielectric layer with respect to the normal of the boundary. The real part of $\delta$ is the electrical length of the path of the wave inside of the dielectric medium. The field reflection coefficient including the multiple reflections inside the layer is

$$R = \frac{r(1-e^{j2\delta})}{1-r^2 e^{-j2\delta}}. \tag{3-5}$$

Equations as (3-3) and (3-5) for an arbitrary number of dielectric layers can be derived using signal flow diagram analysis. In Fig. 3-1, transmission (3-3) and reflection (3-5) of a brick wall with thickness 13 cm and $\varepsilon_r$ = 4.1–j0.15 [P5] are shown at 5.3 GHz. Transmission coefficient changes only slightly when $\phi$ = 0–50°. The reflection coefficients are different for the two polarizations: in the vicinity of the Brewster's angle, $R_\parallel \approx 0$. In [51] power in NLOS corridor for VP polarization was found to be several decibels higher compared to HP. This was because HP (parallel polarization component with respect to the walls) has substantially higher loss by reflection from wall to wall due to the Brewster's angle. In LOS, differences were not found because the corridor structure is roughly symmetrical for VP and HP.
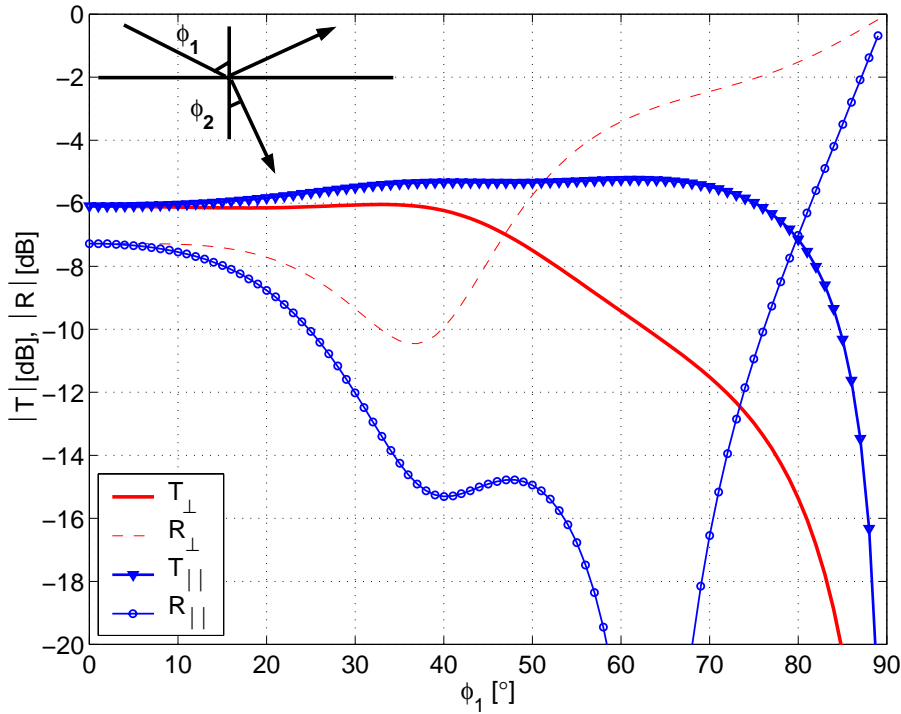


Fig. 3-1. Transmission and reflection coefficients of a dielectric layer, thickness 13 cm, $\varepsilon_r$ = 4.1–j0.15, $f$ = 5.3 GHz.

### 3.1.4 Diffraction

Electromagnetic energy propagates behind edges and wedges, although the transmission through the obstacle would be zero. This is due to diffraction. Diffraction is analyzed according to Huygens' principle, which states that propagation of a wave can be calculated from equivalent sources. The Fresnel-Kirchoff theory gives the scalar value of the field behind an ideally conducting knife-edge, e.g. [52]. In ray theory, complex diffraction coefficients derived using uniform theory of diffraction (UTD) can be used combined with the transmission and reflection coefficients (3-3) and (3-5). In [P5], UTD [53] was used to estimate diffraction to NLOS through a doorway, which was modeled as two knife-edges. The estimated diffraction loss was about 25 dB, which coincides with the directional measurements in [P5]. For modeling of lossy wedges, heuristic equations are given in [54].

### 3.1.5 Scattering

The importance of diffuse scattering in micro- and picocells has been discussed over recent years, e.g. [55]. In [P6], it was found that scattering from building structures, like vertical steel bars inside plasterboard walls, explains certain measurement results. Theory of scattering is known from radar engineering. The pathloss of a scattering ray from A to C (Fig. 3-2) is

$$PL = \left[ \left( \frac{G_1}{4\pi R_{AB}^2} \right) \cdot \sigma(\phi_1, \phi_2, \theta_1, \theta_2) \cdot \left( \frac{G_2}{4\pi R_{BC}^2} \right) \right]^{-1}, \qquad (3\text{-}6)$$

where $\sigma(\phi_1, \phi_1, \theta_1, \theta_2)$ is the bistatic radar cross section of the object, angles $\phi_1, \phi_1, \theta_1,$ and $\theta_2$ are defined in Fig. 3-2. Radar cross sections of objects can be derived (e.g. [56] and [57]) using equivalent sources, which result in secondary apertures, as in the case of diffraction.
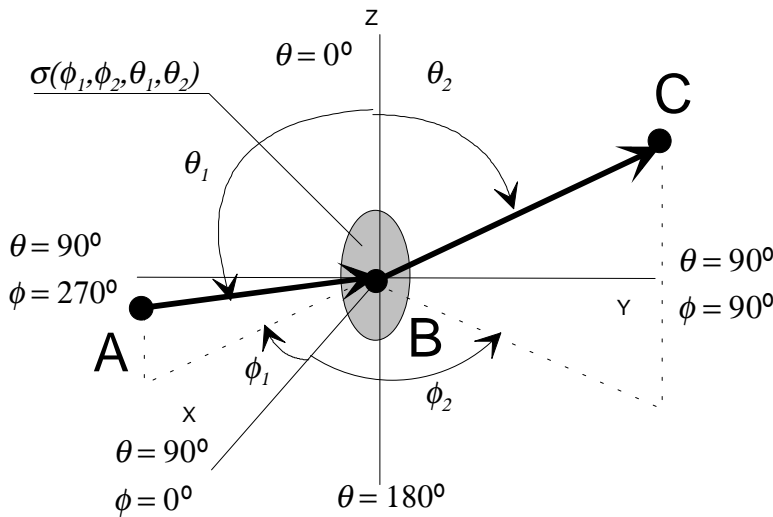


Fig. 3-2. Scattering.

In principle, reflections from rough surfaces are composed of both specular (3-5) and diffuse (3-6) components. A surface is defined rough, when the rms value of the roughness $\sigma_h$ exceeds the Rayleigh criterion for a smooth surface $k \cdot \sigma_h \cdot \sin(\gamma) < \pi/16$, where $k$ is the wavenumber. In [58], measurements at 60 GHz frequency range show that the diffuse component of a reflection from a dielectric plate in the xy-plane has nearly uniform distribution in the xz-plane ($\phi_1 = 0°$) of Fig. 3-2. Obviously, depolarization takes place in the scattering process. Actually, the radar cross section should be defined with orthogonal polarizations, and include crosspolarization.

### 3.1.6 Guided waves

We can see from Fig. 3-1, that when $\phi$ is near 90°, the reflection loss becomes small. Thus the energy can propagate by reflections between the wall and ceiling structures, as in a waveguide. To demonstrate the complexity of the guided wave phenomenon, two reflections at maximum in a corridor structure are shown in Fig. 3-3. The corner reflections are also considered double reflections. Thus we can find 13 separate rays. In average, the resulting pathloss is significantly lower than the free-space pathloss, as seen in the measurements in [P6]. In rigorous calculation of the field, depolarization must be taken into account. In the general case, all reflections have parallel and perpendicular field components. This is especially significant when reflections occur from both the vertical and horizontal structures, which is the case for the rays 10 -13 of Fig. 3-3 b.



a)                                                          b)
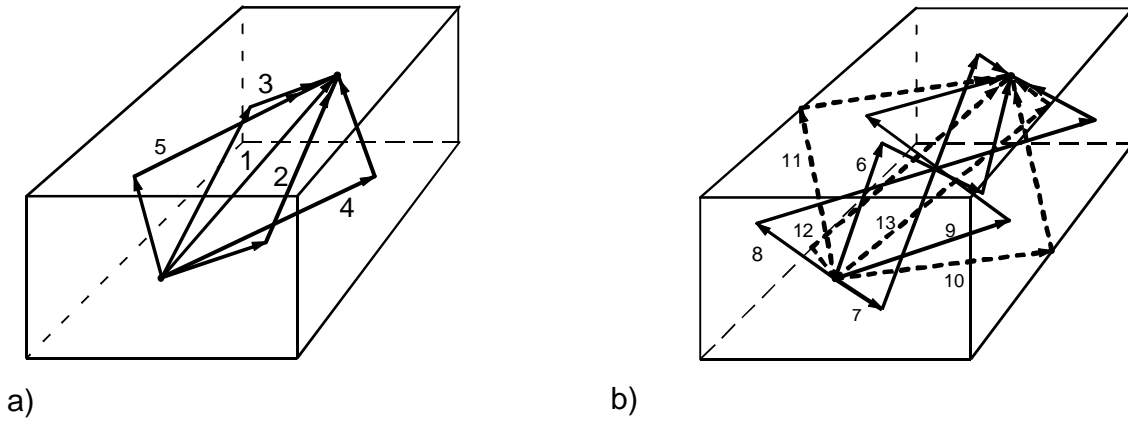
Fig. 3-3. Rays with maximum two reflections contributing to the received signal in a corridor a) LOS and single reflections b) double reflections.

## 3.2  Analysis of the measurement data

### 3.2.1  Characterization of pathloss

As shown in Section 3.1, several mechanisms affect the signals that propagate inside buildings. Ray-tracing is one of the widest used prediction tools in indoor environment, see e.g. [7] and [8]. Modeling of diffraction and diffuse scattering with ray-tracing is a shortage of that principle. Consequently, empirical and semi-empirical modeling is required. In addition, measurement results are needed in the calibration and verification of the deterministic models. In pathloss analysis, measurement results are fitted to an empirical or semi-empirical model on the basis of least mean square error.

#### 3.2.1.1  Motley Keenan model

The Motley-Keenan model [59] suggests, that the average pathloss $PL(d)$ as a function of distance $d$ can be estimated from the free-space pathloss $PL_0(d)$ and from the number of walls $I$ between TX and RX

$$PL(d) = PL_0(d) + \sum_{i=1}^{I} L_{wi}, \tag{3-7}$$

where $L_{wi}$ is the attenuation of wall $i$. The wall attenuation is not the same that could be calculated

by (3-5). Actually, a bookshelf full of paper can have higher attenuation than the wall. Moreover, $L_w$ must include the other propagation mechanisms described in Section 3.1. The accuracy of (3-7) has been improved by dividing walls in different classes and increasing the number of empirical factors in the model ([60], p. 176). In the analysis of the measurements in [P5], it was found that the excess attenuation decreases along with the number of walls in the 'hard wall' environment (Fig. 3-4). The reasons for this are diffraction through doorways and propagation paths outside of the building.
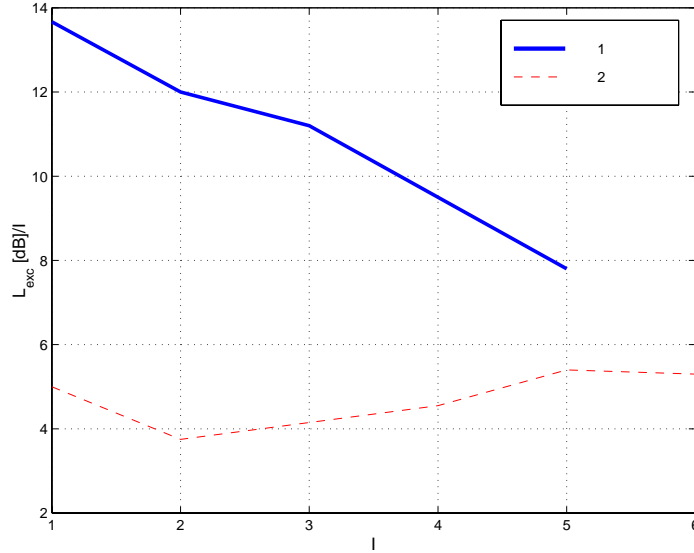


Figure 3-4. Extracted wall attenuation in the hard "1" and light "2" wall environments [P5].

### 3.2.1.2 Log-distance model

The log-distance pathloss model is

$$PL(d) = PL_0(d_0) + 10n \log\left(\frac{d}{d_0}\right) + X_\sigma , \qquad (3-8)$$

where $n$ is the pathloss exponent, $X_\sigma$ is a zero mean log-normally distributed random variable, and $d_0$ the free-space pathloss $PL_0$ distance (in this work, $d_0$ equals 1 meter for comparability). The physical interpretation of $n = 1$ is a guided wave in one plane, $n = 2$ corresponds to a free space pathloss, and $n = 4$ corresponds to a situation, where low antenna heights cause the first Fresnel zone to be obstructed [6]. The distance where the transition from $n = 2$ to $n = 4$ takes place is referred to as the breakpoint. The free space pathloss includes the gains of the antennas (3-1).

The least mean square error of the wideband pathloss, i.e. STD (in dB) of $X_\sigma$, is

$$STD = \sqrt{\frac{1}{N} \cdot \sum \left(10 \log(P_r(x)) + PL(d(x))\right)^2} , \qquad (3-9)$$

where $d(x)$ is the distance at point $x$ and $N$ the number of points. The relative received power $P_r$ is obtained from $h(\tau, x)$ by the following equation

$$P_r(x) = \alpha_{wb} \cdot \int_{\tau_{min}}^{\tau_{max}} |h(\tau, x)|^2 d\tau , \qquad (3-10)$$

where $\alpha_{wb}$ is obtained from the calibration measurement, and $\tau_{min}$ and $\tau_{max}$ are the delays of the first and last detectable IR components, respectively. In [P6] the variance for large scale fading was extracted by averaging $P_r$ over 25 $\lambda$.

30

### 3.2.2 Small scale characterization

### 3.2.2.1 Delay spread

The performance of the modulation schemes used in previous generations of mobile radio systems in the multipath propagation environment can be estimated from values of the rms delay spread $\sigma_\tau$ [61], which is the second central moment of the power delay profile (PDP). In [P6], cumulative distribution functions for the instantaneous values for each impulse response are calculated for each setup.

### 3.2.2.2 Angular spread

In [P5], the rms angular spread in two dimensions is calculated by

$$\sigma_\phi = \sqrt{\frac{\sum_{\phi-\pi}^{\overline{\phi}+\pi} (\phi - \overline{\phi})^2 \cdot P_r(\phi)}{\sum_{\phi-\pi}^{\overline{\phi}+\pi} P_r(\phi)}} \;, \tag{3-11}$$

where $P_r(\phi)$ is obtained by maximum ratio combining (3-10) and $\overline{\phi}$ is the mean incident angle of the power. In comparison with other publications, it must be noted, that in (3-11) the effect of antenna radiation pattern is not reduced from the measurement results. Also, power is integrated over $-\pi$ to $\pi$. Thus the angular spread is $\pi/\sqrt{3}$, when scatterers have a uniform distribution.

### 3.2.2.3 Spatial correlation

Spatial correlation matrix can be used in statistical simulations of antenna arrays [62]. Consider a signal $v(t,x)$, at time $t$ and position $x$. The spatial correlation with distance $\Delta x = x_2 - x_1$ is expressed as

$$\rho(\Delta x) = \left\langle v(t, x_1) \cdot v^*(t, x_2) \right\rangle, \tag{3-12}$$

which includes both the amplitude and phase. The correlation of envelopes of the signals can be calculated as [63]

$$\rho_e(\Delta x) = \left\langle \frac{\left[ |v(t, x_1)| - \overline{|v(x_1)|} \right] \cdot \left[ |v(t, x_2)| - \overline{|v(x_2)|} \right]}{\sqrt{\left( |v(t, x_1)| - \overline{|v(x_1)|} \right)^2 \cdot \left( |v(t, x_2)| - \overline{|v(x_2)|} \right)^2}} \right\rangle. \tag{3-13}$$

In a narrowband Rayleigh fading channel, resulting from complex Gaussian process (uncorrelated phase), normalized (3-12) and (3-13) are related by [63], [64]

$$\rho_e \approx |\rho|^2. \tag{3-14}$$

The same envelope correlation is obtained by using power instead of voltage in [63]. The

correlation function can be calculated from the spatial distribution of the scatterers (with assumptions above). Two-dimensional omnidirectional scattering gives [65]

$$\rho_e(\Delta x) = J_0^2(k \cdot \Delta x), \qquad (3-15)$$

where $J_0$ is the zeroth order Bessel function of the first kind, and $k$ is the wavenumber. When scattering results from a certain direction, as is the case of the base station model for a macrocell, higher correlation values are obtained ([65], p. 62). In omnidirectional 3-D scattering, correlation function is sinc-shaped [66]. In [P6] we use the formulation given in [67] to extract the average normalized spatial correlation ( ~ square root of the envelope correlation) on a stretch from $x_1$ to $x_2$ as a function of distance $\Delta x$

$$R_{av}(\Delta x) = \frac{1}{x_2 - x_1} \cdot \int_{x_1}^{x_2} \frac{1}{\sqrt{E(x)E(x+\Delta x)}} \cdot \left| \int_{\tau_{min}}^{\tau_{max}} h(\tau, x) \cdot h^*(\tau, x+\Delta x) d\tau \right| dx, \qquad (3-16)$$

where energy received at each point $E(x) = P_r(x)/\alpha_{wb}$ from (3-10). The NLOS correlation values in [P6] are significantly higher than (3-15) with distances of several wavelengths, and the mainlobe of the correlation is also slightly wider. This indicates, that instantaneous scattering is not truly omnidirectional.

### 3.2.2.4  Frequency correlation

In a similar way, correlation in frequency domain can be presented for $V(f)$, which is the Fourier-transform of $v(t)$

$$\rho(\Delta f) = \langle V(t, f_1) \cdot V^*(t, f_2) \rangle. \qquad (3-17)$$

Theoretical models are given for an exponentially decaying PDP [4]. Using the formulation of [65], the envelope correlation can be written

$$\rho_e(\Delta f) = \frac{1}{1 + (2\pi\Delta f \sigma_\tau)^2}, \qquad (3-18)$$

where $\sigma_\tau$ is the rms delay spread of the average PDP. The curves in [P6] approximately fit in this model. The general criteria for diversity $\rho_e = 0.7$ ($|\rho| = 0.84$) [64] gives correlation bandwidths between 1- 7 MHz in the described environments. However, in the literature, different criteria for the correlation bandwidth are given.

### 3.2.2.5  Implications on spatial diversity

Because the spatial correlation extracted from measurements is higher than predicted by (3-15), the diversity gain is lower than predicted by this generally used model. Ideal Rayleigh fading with zero correlation gives 13 dB diversity gain in a narrowband system for two-branch diversity (reliability level of 0.99) in maximum ratio combining [64], while curves in [P6] (adding the 3 dB gain compared to single branch) give 1-2 dB less, although the distance is several wavelengths. However, considering the general criteria for diversity gain it is obvious that significant diversity gain can be achieved with antenna separation of only fraction of the wavelength in NLOS. In this analysis, the mutual coupling between the antenna elements, considered important in [64], was omitted.

It has to be noted, that a radio system having wider bandwidth than the correlation bandwidth can-

not obtain the same amount of antenna diversity as a narrowband system, because the total number of diversity branches has to be taken into account (e.g., [65], p. 319).

## 3.3 Empirical modeling

Equations (3-12) and (3-17) give a statistical small scale model of a wide-sense stationary uncorrelated scattering (WSSUS) radio channel - the time correlation function gives the time variation and frequency correlation function the frequency selectivity [4]. For practical applications, like channel simulators, simple models to synthesize the channel have to be developed. In [P6], models with four discrete taps in the delay domain were developed adapting principles described in [68].

The model has the distance dependence of the pathloss depending on the RX-TX configuration, variance for large scale fading, and finally, the small-scale model for multipath propagation. The complete model is depicted in Fig. 3-5. The output of the channel $w(t)$ is obtained by

$$w(t) = \sqrt{PL(t) \cdot \varepsilon_{ls}(t)} \cdot \sum_{m=1}^{N} \sum_{\gamma=f_{D_{\min}}}^{f_{D_{\max}}} z(t - \tau_m) \cdot e^{j2\pi\gamma t} U(\tau_m, \gamma), \qquad (3\text{-}19)$$

where $\varepsilon_{ls}(t)$ describes the large scale fading, $N$ is the number of taps and $U(\tau_m, \gamma)$ is the delay Doppler function (i.e. scattering function) of the radio channel [69]

$$U(\tau_m, \gamma) = \int_{-\infty}^{\infty} h(\tau_m, t) e^{-j2\pi\gamma t} dt \qquad , \qquad (3\text{-}20)$$

where $\gamma$ is the Doppler frequency. The delay Doppler function is extracted from the measurement data as described in [P6].
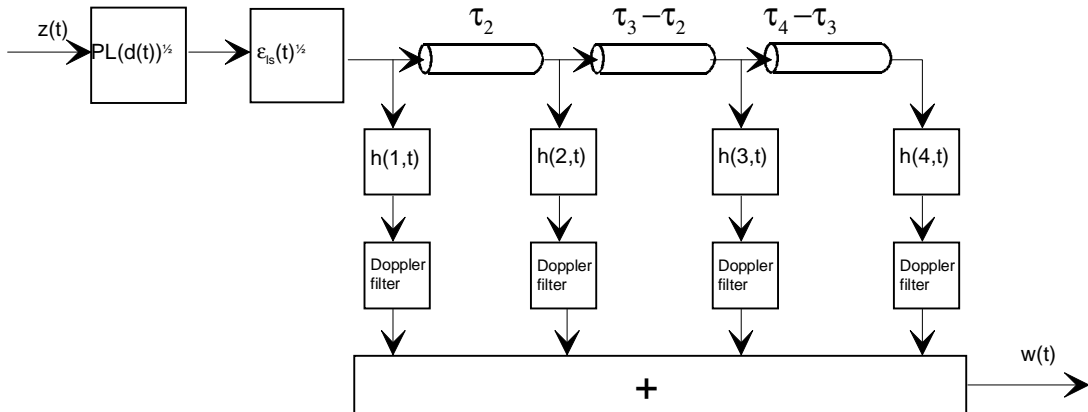


Fig. 3-5. Empirical radio channel model with four taps.

## 3.3.1 Amplitude modeling

Mean values for the taps are calculated from the average PDPs of the datasets. The amplitude distributions of the taps are modeled assuming that the multipath propagation is a complex Gaussian process, as in several references, see e.g. [14], [63], [65], and [70]. Physical interpretation is that the multipath component of each tap results from Gaussian distributed amplitudes that sum with independent phases, resulting in a Rayleigh distributed narrowband signal. If a dominant component is present the distribution becomes Rician [71].

Low correlation values between the taps reflect that the uncorrelated scattering is a reasonable assumption in NLOS cases.

### 3.3.2  Modeling of the Doppler spectrum

The time dependency is modeled by Doppler spectrum, which is theoretically the Fourier transform of (3-12). In the model, Doppler spectra of the taps are classified into classical, Rice [3] and flat [66]. Classical spectrum is derived from uniform distribution of scatterers in azimuth plane [65]. In [P6], higher values of correlation functions compared to these theoretical models were found. Therefore, in indoor environment, the scattering is not truly omnidirectional. The classical or flat shape of the spectrum results from the averaging of large amount of measurement data, which has non-uniform instantaneous spatial distribution of scatterers (Section 3.2.2.3).

## 4    Summary of publications

Paper [P1] describes the requirements of a channel sounding system, and the realized measurement system of HUT at 2 GHz frequency range both at the conceptual and practical level. The realization includes the analog detection of IR using the sliding correlator, and digital detection by post processing using the direct sampling principle. Limitations and accuracy of the measurement are discussed. The available bandwidth limits the achievable unambiguous delay resolution- the code autocorrelation limits the dynamic range in direct sampling, and phase noise limits the Doppler resolution and arrival time uncertainty. Examples of the measurements in train tunnels are given. Although the sliding correlator is widely used due to its simplicity, the described DSP receiver is recommended for real-time measurements. The drawback of the DSP receiver is the limited memory of the sampling boards, which limits the route length of a measurement. Dynamic range of 30 dB was achieved in real measurements. The described system forms the basis for extensions to 5 and 60 GHz frequency ranges and two- and three-dimensional DOA estimations with multi-element antennas.  The limitation of the memory size to the route length has been partly resolved after publication of [P1].

In paper [P2], effects of phase noise on the dynamic range of the direct sequence based wideband channel sounder are evaluated. A closed-form expression for the dynamic range is derived using the rms value of phase noise. The effect of phase noise is negligible for low microwave frequency ranges with typical phase-locked oscillators. At 60 GHz, a slight deterioration of the dynamic range is expected, when phase-locked Gunn-oscillators are used as local oscillators.

Paper [P3] suggests a calibration scheme for virtual antenna array measurements. The virtual array is scanned twice in opposite directions to remove the frequency offset of the synthesizers from the DOA estimation. Uncertainty of the direction of arrival is derived from the Allan variance of the frequency synthesizers, which can be calculated from the spectral density of phase fluctuations. The effect of deadtime between the calibration and the measurement is calculated by using the bias function corresponding to different processes of the noise of the frequency synthesizers. It is shown that measurements with virtual array can be performed without a cable connection between the RX and TX with the 5.3 GHz channel sounder. The errors are of the order of a fraction of a degree.

In paper [P4], the sounder extension to 5.3 GHz is presented. Measurements in indoor environments were performed using the sliding correlator configuration. The origins of components of impulse responses in LOS corridor are analyzed using the delay Doppler domain of the radio channel. Several components were due to multiple reflections from the corridor ends. The cumulative distribu-

tion function of the instantaneous rms delay spread of time-variant radio channel in LOS corridor is presented. Owing to the recent standardization of fourth generation wireless systems, such as HIPERLAN, characterization of the radio channel in frequency and spatial domains is today more important.

Paper [P5] presents directional measurements in two office environments at 5.3 GHz performed by rotating a directive antenna. Dominating propagation mechanisms in NLOS are analyzed: propagation trough walls, coupling through doorways and windows explained by diffraction- and outside propagation paths are found. Delay spread and angular spread of the spatial IRs are analyzed. It is observed that in a hard wall environment signal components arrive from all directions, thus the angular spread is high. Pathloss models applying the Motley-Keenan and log distance models are extracted. When several walls are between the RX and TX, diffraction through doorways and outside propagation paths start to dominate the received signal level, especially in the 'hard wall' environment. Therefore, constant wall attenuation cannot be generally used in the Motley-Keenan model. Further, the wall attenuation in the model cannot be the same as the transmission loss of the wall structure, because propagation through walls was largely affected by the furniture.

In paper [P6], empirical models are developed for typical office environments at 5.3 GHz based on measurements in four different buildings with mainly omnidirectional antennas. Pathloss is characterized by the log-distance pathloss exponent and standard deviation between measurement and model. Pathloss exponent is about 1.4 in all LOS cases, which is due to the wave guiding effects resulting from wall, floor and ceiling reflections. In the NLOS case, the difference in the pathloss models in different buildings was significant. Delay spreads and correlation functions for NLOS in space and frequency domains are extracted. Behavior of the spatial diversity was estimated on the basis of spatial correlation functions extracted from the measurement data; an antenna separation of a fraction of a wavelength can give significant diversity gain in indoor environments at 5.3 GHz in NLOS. Small-scale models are developed by combining the data from different buildings for similar set-ups; and extracting the mean amplitude, amplitude distribution, delay, and Doppler spectrum of four taps. Doppler spectra indicate, that in certain cases scatterers also have a significant spread in the elevation plane.

Paper [P7] presents the results of an extensive measurement campaign at 5.3 GHz in different outdoor environments and with different antenna heights using the direct sampling configuration. Pathloss and delay spread are analyzed. Diffraction over the rooftops gives better coverage in NLOS in urban environments when the base station antenna is above the rooftop level, rather than at the heights of the lower base station antenna. However, the delay spread also increases along with the antenna height. In rural environment, effects of vegetation were found significant: excess attenuation was 5-10 dB higher at summertime compared to wintertime.

## 5    Conclusions

In this thesis, measurement techniques for wideband radio channels for future radio systems were studied at 2-60 GHz frequency range. Partly in this thesis, a radio channel measurement system with 100 MHz bandwidth was designed and completed at 2.154 GHz. The work that was not included in [P1] comprises the design of the fast ECL based code generators and redesign of the IQ-demodulator, AGC, and PLL, in order to improve the reliability of the system. The extensions to 5.3 and 60 GHz center frequencies, of which the 5.3 GHz extension is complete, are results of this thesis only. Measurement campaigns were realized at 5.3 GHz, including directional measurements by rotating a directive antenna and continuous measurements with mainly omnidirectional antennas. Propagation mechanisms were studied on the basis of these measurements. Empirical models were

developed.

With the described sounder design, and its later extensions e.g. [25] and [43], several large measurement campaigns have been performed for third and fourth generation wireless system, network and antenna studies (e.g. [P6], [P7], [44], [72] - [78]). Therefore, results of this work have been fruitful, and the sounder gives scientific information, that has not previously been available in mobile communications research. Furthermore, the developed sounder has been used as a prototype of a commercial product.

It has been shown in this thesis, that the measurement system design, including the 2-D and 3-D measurements, until today mainly applied in the 2 GHz range due to the emerging UMTS system, can be applied up to the 60 GHz range, at least from the electronics point of view. The major technical problems are the limitations of transmitter power due to amplifier technology and the phase noise. It is shown by theoretical analysis that, when the measurement time is limited, the errors due to phase noise can be tolerated, provided that the ultra low-noise frequency synthesis using multiplied DRO and calibration principle described in this thesis are applied.

It is shown that semi-empirical modeling principles generally applied at lower frequencies in indoor radio channel are not directly applicable at the 5 GHz frequency range. This is because the absorption loss of a dielectric medium can be notably higher at 5 GHz, and the dominating propagation mechanisms may be different e.g. at 1 and 5 GHz frequencies. For example, coupling via openings in building structures, which is explained by diffraction, is significant at 5 GHz. In NLOS, Rayleigh fading narrowband channel is found. Achievable antenna diversity gain 1-2 dB less than the theoretical model in [65] was estimated, omitting the mutual coupling between the elements. It may be seen that the difference is due to the assumption of the uniform distribution of scatterers used in the theoretical model.

Finally, a straightforward way of generating statistical models from the measurement data was applied. Pathloss exponent is less than the free space pathloss in LOS situations due to wave guiding. A value of about 1.4 was found. In NLOS, the pathloss exponent was different in different buildings varying between 2.6 – 4.8 in office buildings in single floor setups. Doppler spectrum analysis shows that scatterers have significant spread in elevation plane in certain cases. The delay dispersion was characterized by cumulative distribution functions (CDF) of the rms delay spreads, the values for CDF = 0.9 varied from 20 to 180 ns in different set-ups in different office buildings and large hall environments.

**Errata**

In [P1] in the footer of page 1. Manuscript received April 15, 1995 should read Manuscript received April 15, 1998.

In [P2] in the first column. Output power of the active device should read input power of the active device.

In [P2] eq. 12  is                                           should read
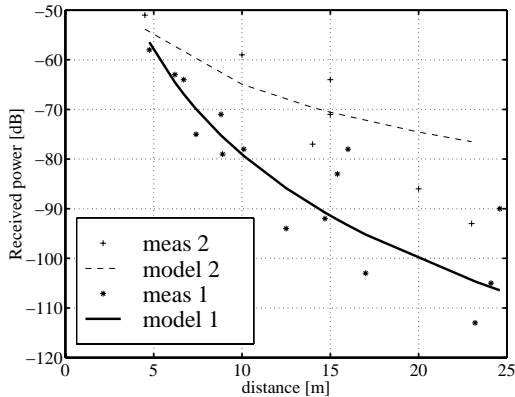
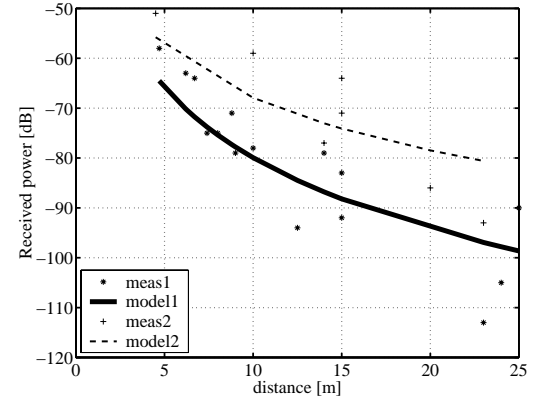$$h(t) = s(t) \otimes r(t) \qquad\qquad h(t) = s(-t) \otimes r(t)$$

In [P4] in equations (3) and (4) $k = 1$ should read $i = 1$.

In [P5], in Table 1 in row 3 column 2 $n = 3.3$ should read $n = 3.5$.

In [P5], in Fig. 9, the upper figure is                    should be



## References

[1]  J. Kivinen, T. Korhonen, J. Hubach, and P. Vainikainen, "Fast sounding of broadband radio channel at 2 GHz frequency range," *Nordic Radio Symposium Proceedings,* 24–27 April 1995, Saltsjöbaden, Sweden, pp. 121–126.

[2]  L. Correia, "An overview of wireless broadband communications," *IEEE Communications Magazine*, vol. 35, No. 1, Jan 1997, pp. 28–33.

[3]  T. Ojanperä and R. Prasad, *"Wideband CDMA for Third Generation Mobile Communications,"* Artech House, USA, 1998, 439 p.

[4]  R. van Nee and R. Prasad, *"OFDM for Wireless Multimedia Communications,"* Artech House, USA, 2000, 260 p.

[5]  J. B. Andersen, "Antenna arrays in mobile communications: gain, diversity, and channel capacity," *IEEE Antennas and Propagation Magazine*, vol. 42, No. 2, April, 2000, pp. 12–16.

[6]  J. B. Andersen, T. S. Rappaport, and S. Yoshida, "Propagation measurements and models for wireless communication channels," *IEEE Communications Magazine*, vol. 33, No.1, Jan. 1995, pp. 42–49.

[7]  A. R. Nix, G. E. Athanasiadou, J. P. McGeehan, "Predicted HIPERLAN coverage and outage performance at 5.2 and 17 GHz using indoor 3-D ray-tracing techniques," *Wireless Personal Communications*, 1996, No. 3, pp. 365–388.

[8]  W. M. O'Brien, E. M. Kenney, and P. J. Cullen, "An efficient implementation of a three-dimensional microcell propagation tool for indoor and outdoor environments," *IEEE Transactions on Vehicular Technology*, vol. 49, No. 2, March 2000, pp. 622–630.

[9]  P. J. Cullen, P. C. Fannin, and A. Garvery, "Real-time simulation of randomly time-variant linear systems: the mobile radio channel," *IEEE Transactions on Instrumentation and Measurement*, vol. 43, No. 4, Aug. 1994, pp. 583–591.

[10] A. Hewitt and E. Vilar, "Selective fading on LOS microwave links: classical and spread-spectrum measurement techniques, " *IEEE Transactions on Communications*, vol. 36, No. 7, July 1988, pp. 789–796.

[11] J. D. Parsons, D. A. Demery, and A. A. D. Turkmani, "Sounding techniques for wideband mobile radio channels: a review," *IEE Proceedings–I,* vol. 138, No. 5, Oct. 1991, pp. 625–635.

[12] T. S. Rappaport, S. Y. Seidel, and R. Singh, "900-MHz multipath propagation measurements for U.S. digital cellular radiotelephone," *IEEE Transactions on Vehicular Technology*, vol.

39, No. 2, May 1990, pp. 132−139.

[13] S. Guerin, Y.J. Guo, and S.K. Barton, "Indoor propagation measurements at 5 GHz for HIPERLAN," *IEE 10<sup>th</sup> International Conference on Antennas and Propagation Proceedings*, Edinburgh, England, April 1997, pp. 306 –310.

[14] J. Medbo, H. Hallenberg, and J. E. Berg, "Propagation characteristics at 5 GHz in typical radio-LAN scenarios," *Vehicular Technology Conference Proceedings*, Houston, USA, May 16–19, 1999, pp. 185 –189.

[15] P.F.M. Smulders and A.G. Wagemans, "Frequency-domain measurement of the millimeter wave indoor radio channel," *IEEE Transactions on Instrumentation and Measurement*, vol. 44, No. 6, Dec. 1995, pp. 1017–1022.

[16] G. Woodward and J. Talvitie, "Wideband spatial and temporal channel modelling for ISM bands," *COST 259/260 Joint Workshop Proceedings*, 20–21 April, 1999,Vienna, Austria, pp.55–62.

[17] G. Woodward, I. Opperman, and J. Talvitie, "Outdoor-indoor temporal & spatial wideband channel model for ISM bands," *IEEE VTS 50<sup>th</sup> Vehicular Technology Conference Proceedings*, Amsterdam, Netherlands, Sept. 19–22, 1999, pp. 136 –140.

[18] D. C. Cox, "Delay Doppler characteristics of multipath propagation at 910 MHz in a suburban mobile radio environment," *IEEE Transactions on Antennas and Propagation*, vol. 20, No. 5, Sept. 1972, pp. 625−635.

[19] P. Karlsson and L. Olsson, "Time dispersion measurement system for radio propagation at 1800 MHz and results from typical indoor environments," *IEEE VTS 44<sup>th</sup> Vehicular Technology Conference Proceedings*, 1994, pp. 1793 –1797.

[20] Y. L. C. de Jong and M. H. A. J. Herben, "High resolution angle of arrival measurement of the mobile radio channel," *IEEE Transactions on Antennas and Propagation*, vol. 47, No. 11, Nov. 1999, pp. 1677−1687.

[21] P. C. Fannin, A. Molina, S. S. Swords, and P. J. Cullen, "Digital signal processing techniques applied to mobile radio channel sounding," *IEE Proceedings-F*, vol. 138, No. 5, Oct. 1991, pp. 502−508.

[22] A. Molina, P. C. Fannin, and J. Timoney, "Generation of optimum excitation waveforms for mobile radio channel sounding," *IEEE Transactions on Vehicular Technology*, vol. 44, No. 2, May 1995, pp. 275 –279.

[23] S. A. Mohamed, G. Lovnes, E. Antonsen, R. H. Raekken, B. Nigeon, and J. J. Reis, "Report on propagation measurements," *RACE Document*, R2067/BTL/2.2.2/DS/P/035.a1.

[24] A. B. Carlson, "*Communication Systems*," McGraw-Hill Company, Singapore, 1986, 686 p.

[25] K. Kalliola and P. Vainikainen, "Characterization system for radio channel of adaptive array antennas," *International Symposium on Personal, Indoor and Mobile Radio Communications Proceedings*, Helsinki, Finland, Sept 1–4, 1997, pp. 95−99.

[26] A. I. Zverev, "*Handbook of Filter Synthesis*," John Wiley & Sons, Inc., USA, 1967.

[27] T. Dabocz, "Uncertainty of signal reconstruction in the case of jittery and noisy measurements," *IEEE Transactions on Instrumentation and Measurement*, vol. 47, No. 5, Oct. 1998, pp. 1062 –1066.

[28] T. Felhauer, P. W. Baier, W. König, and W. Mohr, "Optimum spread spectrum signals for wideband channel sounding," *Electronics Letters,* vol. 29, No. 6, March 1993.

[29] J. Riska, M. Kärkkäinen, P. Kangaslahti, and V. Porra, "Amplifiers and signal generation circuits for 60 GHz wireless broadband system," *30<sup>th</sup> European Microwave Conference Proceedings*, Paris, France, Oct. 2000.

[30] P.F.M. Smulders and A.G. Wagemans, "Biconical horn antennas for near uniform coverage in indoor areas at mm-wave frequencies," *IEEE Transactions on Vehicular Technology*, vol. 43, No. 4, Nov. 1994, pp. 897–901.

[31] V. F. Kroupa, "Noise properties of PLL systems," *IEEE Transactions on Communications*,

vol. 30, pp. 2244–2252, No. 10, Oct. 1982.

[32] P. Kangaslahti, J. Riska, M. Kärkkäinen, P. Alinikula, and V. Porra, "Low phase noise signal generation circuits for 60 GHz wireless broadband system", *IEEE International Microwave Symposium,* Boston, 2000, pp. 43–46.

[33] L. Walls and D. W. Allan, "Measurements of frequency stability," *Proceedings of the IEEE*, vol. 74, No. 1, 1986, 162–168.

[34] D. W. Allan, "The measurement of frequency and frequency stability of precision oscillators," *NBS technical note 669,* May 1975, 28 p.

[35] J. A. Barnes, A. R. Chi, L. S. Cutler, D. J. Healey, D. B. Leeson, T. E. Mc Gunigal, J. A. Mullen, Jr., W. L. Smith, R. L. Sydnor, R. F. C. Vessot, and G. M. Winkler, "Characterization of frequency stability," *IEEE Transactions on Instrumentation and Measurement*, vol. 20, No. 1, 1971, 105–120.

[36] J. Fuhl, J-P Rossi, and E. Bonek, "High-resolution 3-D direction of arrival determination for urban mobile radio," *IEEE Transactions on Antennas and Propagation*, vol. 45, No. 4, 1997, pp. 672–682.

[37] J. Kivinen and P. Vainikainen, "Analysis of wideband indoor propagation measurements at 5.3 GHz," *COST 259 Temporary Documents TD(67)*, Bradford, England, 1998, 10 p.

[38] M. Zoltowski, M. Haardt, and C. Mathews, "Closed-form 2-D angle estimation with rectangular arrays in element space or beamspace via unitary ESPIRIT, *IEEE Transactions on Signal Processing*, vol. 44, No. 2, 1994, 316–328.

[39] B. Fleury, D. Dalhaus, R. Heddergott, and M. Tschudin, "Wideband angle of arrival estimation using the sage algorithm," *IEEE 4$^{th}$ International Symposium on Spread Spectrum Techniques and Applications Proceedings*, Mainz, Germany, Sept. 22–25, 1996, pp. 79–85.

[40] J. O. Nielsen, G. E. Pedersen, K. Olesen, I. Z. Kovacs, "Computation of mean effective gain from 3D measurements," *IEEE VTS 49$^{th}$ Vehicular Technology Conference Proceedings*, 1999, pp. 787 –791.

[41] P. Karlsson, C. Bergljung, E. Thomsen, and H. Börjeson, "Wideband measurement and analysis of penetration loss in the 5 GHz band," *IEEE VTS 50$^{th}$ Vehicular Technology Conference Proceedings*, Amsterdam, Netherlands, Sept. 19–22, 1999, pp. 2323–2328.

[42] J-P. Rossi, J-P. Barbot, and A. J. Levy, "Theory and measurement of the angle of arrival and time delay of UHF radiowaves using a ring array," *IEEE Transactions on Antennas and Propagation*, vol. 45, No. 5, 1997, pp. 876–884.

[43] K. Kalliola, H. Laitinen, L. I. Vaskelainen, and P. Vainikainen, "Real-time 3D spatial-temporal dual-polarized measurement of wideband radio channel at mobile station", *IEEE Transactions on Instrumentation and Measurement*, vol. 49, No. 2, April 2000, pp. 439–448.

[44] K. Kalliola, J. Laurila, M. Toeltsch, K. Hugl, P. Vainikainen, and E. Bonek, "3-D directional wideband dual-polarized measurement of urban mobile radio channel with synthetic aperture technique," *Millennium Conference on Antennas and Propagation Proceedings*, CD-ROM SP-444 (ISBN 92-9092-776-3), Davos, Switzerland, April 9-14, 2000, session 2p1, paper No. 873.

[45] R. S. Thomä, D. Hampicke, A. Richter, G. Sommerkorn, A. Schneider, and U. Trautwein, "Identification of time-variant directional mobile radio channels," *16$^{th}$ IEEE Instrumentation and Measurement Technology Conference Proceedings,* Venice, Italy, May 24–26, 1999, pp.176–181.

[46] G. Martin, "Wideband channel sounding dynamic range using a sliding correlator," *IEEE VTS 51$^{st}$ Vehicular Technology Conference Proceedings*, Tokyo, Japan, May 5–18, 2000, pp. 2517–2521.

[47] R. McDonough, "*Detection of Signals in Noise*," Second Edition, Academic Press, USA, 1995, 495 p.

[48] L. E. Larson, "*Microwave and RF Circuit Design for Wireless Communications*," Artech

House Inc., Norwood MA, 1996, 411 p.

[49] T. S. Rappaport, "*Wireless Communications, Principles and Practice*" Prentice Hall Inc., Upper Saddle River, NJ, 1996, 641 p.

[50] E. Nyfors and P. Vainikainen, "*Industrial Microwave Sensors*," Artech House Inc., Norwood MA, 1989, 351 p.

[51] J. Kivinen and P. Vainikainen, "Wideband propagation measurements in corridors at 5.3 GHz," *IEEE 5th International Symposium on Spread Spectrum Techniques and Applications Proceedings*, Sun City, South Africa, Sept. 2–4, 1998, pp. 512–516.

[52] H. Mokhtari and P. Lazaritis, "Comparative study of lateral profile knife-edge diffraction and ray tracing technique using GTD in urban environment," *IEEE Transactions on Vehicular Technology*, vol. 48, No. 2, March 1999, pp. 589 –592.

[53] W. L. Stutzman and G. A. Thiele, "*Antenna Theory and Design*," John Wiley & Sons, Inc., USA, 1981, 598 p.

[54] R. J. Luebbers, "A heuristic UTD slope diffraction coefficient for rough lossy wedges," *IEEE Transactions on Antennas and Propagation*, vol. 37, No. 2, Feb. 1989, pp. 206–211.

[55] V. Degli-Esposti and H. L. Bertoni, "Evaluation of diffuse scattering in urban microcellular propagation," *IEEE VTS 50th Vehicular Technology Conference Proceedings*, Amsterdam, Netherlands, Sept. 19–22, 1999, pp. 1392–1396.

[56] D. R. Wehner "*High Resolution Radar*," Artech House, Inc., Norwood M.A., 1987, 472 p.

[57] M. Skolnik, "*Radar Handbook*," McGraw-Hill, New York, USA, 1970, 1536 p.

[58] L. M. Correia, P. O. Frances, J. R. Reis, J. M. Brazio, F. V. Velez, W. Herzig, P. H. Lehne, J. Fernandez, and C. Plenge, "Final report on propagation aspects," *RACE Document* R2067/IST/2.2.5/DS/P/070.b1.

[59] J. M. Keenan and A. J. Motley, "Radio coverage in buildings," *British Telecom Technology Journal*, vol. 8, No. 1, Jan. 1990, pp. 19–24.

[60] E. Damosso, L. Correia (ed.), "*Digital Mobile Radio Towards Future Generation Systems*," Cost 231 Final Report, Belgium 1999, 474 p.

[61] J. C-I. Chuang, "The effects of time delay spread on portable radio communications channels with digital modulation," *IEEE Journal on Selected Areas in Communications*, vol. 5, No. 5, June 1987, pp. 879–889.

[62] J. C. Liberti and T. S. Rappaport, "Analysis of CDMA cellular radio systems employing adaptive antennas in multipath environments," *IEEE VTS Vehicular Technology Conference Proceedings, Atlanta*, USA, 1996, pp. 1076 –1080.

[63] J. R. Pierce and S. Stein, "Multiple diversity with nonindependent fading," *Proceedings of the IRE*, vol. 48, 1960, pp. 89–104.

[64] R. G. Vaughan and J. B. Andersen, "Antenna diversity in mobile communications," *IEEE Transactions on Vehicular Technology*, vol. 36, No. 4, Nov. 1987, pp. 149–172.

[65] W. C. Jakes, "*Microwave Mobile Communications*," John Wiley & Sons, Inc., USA, 1974, 642 p.

[66] R. H. Clarke and W. Lin Khoo, "3-D mobile radio channel statistics," *IEEE Transactions on Vehicular Technology*, vol. 46, No. 3, Aug. 1997, pp. 798–799.

[67] U. Dersch and E. Zollinger, "Physical characteristics of urban micro-cellular propagation," *IEEE Transactions on Antennas and Propagation*, vol. 42, No. 11, November 1994, pp. 1528–1539.

[68] W. Mohr, "Modeling of wideband mobile radio channel based on propagation measurements," *International Symposium on Personal, Indoor and Mobile Radio Communications Proceedings*, Toronto, Canada, Sept. 27–29, 1995, pp. 397–401.

[69] P. A. Bello, "Characterization of randomly time-variant linear channels," *IEEE Transactions On Communications Systems*, vol. 11, Dec. 1963, pp. 360–393.

[70] L. Dossi, G. Tartara, and F. Tallone, "Statistical analysis of measured impulse response func-

tions of 2.0 GHz indoor radio channels," *IEEE Journal on Selected Areas in Communications*, vol. 14, No. 3, April 1996, pp. 405–410.

[71]  S. O. Rice, "Statistical properties of a sine wave plus random noise," *Bell System Technical Journal*, vol. 27, Jan. 1948, pp. 109–157.

[72]  P. Vainikainen, P. Aikio, R. Gruber, M. Hall, P. Degauque, M. Lienard, M. Berbineau, M. Szelag, F. Mollet, M. Klingler, W. Pirard, L. Deryck, Y. Verolleman, "Characteristics of the 2 GHz radio propagation channel in high speed train environment," *Proceedings of the ACTS Mobile Communications Summit*, 27-29 November 1996, Granada, Spain, pp. 616-623.

[73]  P. Erätuuli, P. Haapala, P. Aikio, and P. Vainikainen, "Measurements of internal handset antennas and diversity configurations with a phantom head," *IEEE AP-S International Symposium Digest*, Atlanta, USA, June 1998, pp. 145–148.

[74]  P. Haapala, P. Erätuuli, P. Aikio, and P. Vainikainen, "Evaluation of handset antennas in different multipath environments," *IEEE AP-S International Symposium Digest*, Atlanta, USA, June 1998, pp. 126–129.

[75]  K. Karttunen, K. Kalliola, T. Laakso, and P. Vainikainen, "Measurement analysis of spatial and temporal correlation in wideband radio channels with adaptive antenna array," *International Conference on Universal Personal Communications*, Florence, Italy, 5–9 Oct., 1998, pp. 671–675.

[76]  P. Aikio, R. Gruber, and P. Vainikainen, " Wideband radio channel measurements for train tunnels," *IEEE VTS 48th Vehicular Technology Conference Proceedings*, Ottawa, Canada, May 18–21, 1998, pp. 460–464.

[77]  K. Sulonen, K. Kalliola, and P. Vainikainen, "Comparison of evaluation methods for mobile handset antennas," *Millennium Conference on Antennas and Propagation Proceedings*, CD-ROM SP-444 (ISBN 92-9092-776-3), Davos, Switzerland, April 9–14, 2000, paper No. 870.

[78]  A. T. Alastalo, A. Väisänen, K. Leppänen, K. Kalliola, M. E. Ermutulu, and A. Brehonnet, "Adaptive antennas for wireless local area networks," *Millennium Conference on Antennas and Propagation Proceedings*, CD-ROM SP-444 (ISBN 92-9092-776-3), Davos, Switzerland, April 9–14, 2000, session 5a5, paper No. 1102.